

Numerical Studies of the 2D Hubbard Model

D.J. Scalapino

Department of Physics, University of California, Santa Barbara, CA 93106-9530, USA

Abstract

Numerical studies of the two-dimensional Hubbard model have shown that it exhibits the basic phenomena seen in the cuprate materials. At half-filling one finds an antiferromagnetic Mott-Hubbard groundstate. When it is doped, a pseudogap appears and at low temperature d-wave pairing and striped states are seen. In addition, there is a delicate balance between these various phases. Here we review evidence for this and then discuss what numerical studies tell us about the structure of the interaction which is responsible for pairing in this model.

1. Introduction

A variety of numerical methods have been used to study Hubbard and t-J models and there are a number of excellent reviews. [1–8] The approaches have ranged from Lanczos diagonalization [1, 2, 9–11] of small clusters to density-matrix-renormalization-group studies of n-leg ladders [8, 12–14] and quantum Monte Carlo simulations of two-dimensional lattices [3, 15–24]. In addition, recent cluster generalizations of dynamic mean-field theory [4, 6, 7, 25–33] are providing new insight into the low temperature properties of these models. A significant finding of these numerical studies is that these basic models can exhibit antiferromagnetism,

stripes, pseudogap behavior, and $d_{x^2-y^2}$ pairing. In addition, the numerical studies have shown how delicately balanced these models are between nearly degenerate phases. Doping away from half-filling can tip the balance from antiferromagnetism to a striped state in which half-filled domain walls separate π -phase-shifted antiferromagnetic regions. Altering the next-near-neighbor hopping t' or the strength of U can favor $d_{x^2-y^2}$ pairing correlations over stripes. This delicate balance is also seen in the different results obtained using different numerical techniques for the same model. For example, density matrix renormalization group (DMRG) calculations for doped 8-leg t-J ladders find evidence for a striped ground state. [12] However, variational and Green's function Monte Carlo calculations for the doped t-J lattice, pioneered by Sorella and co-workers, [23, 24] find groundstates characterized by $d_{x^2-y^2}$ superconducting order with only weak signs of stripes. Similarly, DMRG calculations for doped 6-leg Hubbard ladders [14] find stripes when the ratio of U to the near-neighbor hopping t is greater than 3, while various cluster calculations [27, 30–33] find evidence that antiferromagnetism and $d_{x^2-y^2}$ superconductivity compete in this same parameter regime. These techniques represent present day state-of-the-art numerical approaches. The fact that they can give different results may reflect the influence of different boundary conditions or different aspect ratios of the lattices that were studied. The n -leg open boundary conditions in the DMRG calculations can favor stripe formation. Alternately, the cluster lattice sizes and boundary conditions can frustrate stripe formation. It is also possible that these differences reflect subtle numerical biases in the different numerical methods. Nevertheless, these results taken together show that both the striped and the $d_{x^2-y^2}$ superconducting phases are nearly degenerate low energy states of the doped system. Determinantal quantum Monte Carlo calculations [21] as well as various cluster calculations show that the underdoped Hubbard model also exhibits pseudogap phenomena. [27–32] The remarkable similarity of this behavior to the range of phenomena observed in the cuprates provides strong evidence that the Hubbard and t-J models indeed contain a significant amount of the essential physics of the problem. [34]

In this chapter, we will focus on the one-band Hubbard model. Section 2 provides an

overview of the numerical methods which were used to obtain the results that will be discussed. We have selected three methods, determinantal quantum Monte Carlo, the dynamic cluster approximation and the density-matrix-renormalization group. In principle, these methods provide unbiased approaches which can be extrapolated to the bulk limit or in the case of the DMRG, to “infinite length” ladders. This choice has left out many other important techniques such as the zero variance extrapolation of projector Monte Carlo, [23, 24], variational cluster approximations, [25, 26, 29–32] renormalization group flow techniques, [35–37] high temperature series expansions [38–40] and the list undoubtedly goes on. It was motivated by the need to write about methods with which I have direct experience.

In Section 3 we review the numerical evidence showing that the Hubbard model can indeed exhibit antiferromagnetic, $d_{x^2-y^2}$ pairing and striped low-lying states as well as pseudogap phenomena. From this we conclude that the Hubbard model provides a basic description of the cuprates, so that the next question is what is the interaction that leads to pairing in this model? From a numerical approach, this question is different from determining whether the groundstate is antiferromagnetic, striped, or superconducting. Here, one would like to understand the structure of the underlying effective interaction that leads to pairing. Although on the surface this might seem like a more difficult question to address numerically, it is in fact easier than determining the nature of the long-range order of the low temperature phase. The phase determination problem involves an extrapolation to an infinite lattice at low, or in the case of antiferromagnetism, to zero temperature. However, the pairing interaction is short-ranged and is formed at a temperature above the superconducting transition so that it can be studied on smaller clusters and at higher temperatures.

As discussed in Section 4, the effective pairing interaction is given by the irreducible particle-particle vertex Γ^{pp} . Using Monte Carlo results for the one- and two-particle Green’s functions, one can determine Γ^{pp} and examine its momentum and Matsubara frequency dependence. [41, 42] One can also determine if it is primarily mediated by a particle-hole magnetic ($S = 1$) exchange, a charge density ($S = 0$) exchange, or by a more complex mechanism. Section 5 contains a summary and our conclusions.

2. Numerical Techniques

In this chapter we will be reviewing numerical results which have been obtained for the 2D Hubbard model. It would, of course, be simplest if one could say that these results were obtained by “exact” diagonalization on a sequence of $L \times L$ lattices with a “finite-size scaling” analysis used to determine the bulk limit. While one might not know the exact details of how this was done, one understands what it means. Unfortunately the exponential growth of the Hilbert space with lattice size limits this approach and other less familiar and often less transparent methods are required.

In this chapter, we will discuss results obtained using the determinantal quantum Monte Carlo algorithm, [16, 43] a dynamic cluster approximation, [6, 27] and the density matrix renormalization group. [44, 45, 5] All of these methods have been described in detail in the literature. However, to provide a context for the numerical results discussed in Sections 3 and 4, we proceed with a brief overview of these techniques.

Determinantal Quantum Monte Carlo

The determinantal quantum Monte Carlo method was introduced in order to numerically calculate finite temperature expectation values.

$$\langle A \rangle = \frac{\text{Tr } e^{-\beta H} A}{Z}. \quad (1)$$

Here, H includes $-\mu N$ so that $Z = \text{Tr } e^{-\beta H}$ is the grand partition function. For the Hubbard model, the Hamiltonian is separated into a one-body term

$$K = -t \sum_{\langle ij \rangle \sigma} \left(c_{i\sigma}^\dagger c_{j\sigma} + c_{j\sigma}^\dagger c_{i\sigma} \right) - \mu \sum_{i\sigma} n_{i\sigma} \quad (2)$$

and an interaction term

$$V = U \sum_i \left(n_{i\uparrow} - \frac{1}{2} \right) \left(n_{i\downarrow} - \frac{1}{2} \right). \quad (3)$$

Then, dividing the imaginary time interval $(0, \beta)$ into M segments of width $\Delta\tau$, we have

$$e^{-\beta H} = [e^{-\Delta\tau(K+V)}]^M \simeq [e^{-\Delta\tau K} e^{-\Delta\tau V}]^M. \quad (4)$$

In the last term, a Trotter breakup has been used to separate the non-commuting operators K and V . This leads to errors of order $tU\Delta\tau^2$ which can be systematically treated by reducing the size of the time slice $\Delta\tau$. Then, on each $\tau_\ell = \ell\Delta\tau$ slice and for each lattice site i , a discrete Hubbard-Stratonovich field [46] $S_i(\tau_\ell) = \pm 1$ is introduced so that the interaction can be written as a one-body term

$$e^{-\Delta\tau U(n_{i\uparrow} - \frac{1}{2})(n_{i\downarrow} - \frac{1}{2})} = \frac{e^{-\frac{\Delta\tau U}{4}}}{2} \sum_{S_i(\tau_\ell) = \pm 1} e^{-\Delta\tau \lambda S_i(\tau_\ell)(n_{i\uparrow} - n_{i\downarrow})} \quad (5)$$

with λ set by $\cosh(\Delta\tau\lambda) = \exp(\Delta\tau\frac{U}{2})$. The interacting electron problem has now been replaced by the problem of many electrons coupled to a τ -dependent Hubbard-Stratonovich Ising field $S_i(\tau_\ell)$ which is to be averaged over. This average will be done by Monte Carlo importance sampling.

For an $L \times L$ lattice, it is useful to introduce a one-body $L^2 \times L^2$ lattice Hamiltonian $h_\sigma(S(\tau_\ell))$ for spin σ electrons interacting with the Hubbard-Stratonovich field on the τ_ℓ -imaginary time slice

$$\begin{aligned} \sum_{\langle ij \rangle} c_{i\sigma}^\dagger h_\sigma(S(\tau_\ell)) c_{j\sigma} &= -t \sum_{\langle ij \rangle} (c_{i\sigma}^\dagger c_{j\sigma} + c_{j\sigma}^\dagger c_{i\sigma}) \\ -\mu \sum_i n_{i\sigma} &\pm \lambda \sum_i S_i(\tau_\ell) n_{i\sigma}. \end{aligned} \quad (6)$$

The plus sign is for spin-up ($\sigma = 1$) and the minus sign is for spin-down ($\sigma = -1$). Then, tracing out the fermion degrees of freedom, one obtains

$$Z = \sum_{\{S\}} \det M_\uparrow(S) \det M_\downarrow(S). \quad (7)$$

The sum is over all configurations of the $S_i(\tau_\ell)$ field and $M_\sigma(S)$ is an $L^2 \times L^2$ matrix which depends upon this field,

$$M_\sigma(S) = I + B_M^\sigma B_{M-1}^\sigma \cdots B_1^\sigma. \quad (8)$$

I is the unit $L^2 \times L^2$ matrix and $B_\ell^\sigma = e^{-\Delta\tau h_\sigma(S(\tau_\ell))}$ acts as an imaginary time propagator which evolves a state from $(\ell - 1)\Delta\tau$ to $\ell\Delta\tau$.

The expectation value $\langle A \rangle$ becomes

$$\langle A \rangle = \sum_{\{S\}} A(S) \frac{\det M_{\uparrow}(S) \det M_{\downarrow}(S)}{Z} \quad (9)$$

with $A(S)$ the estimator for the operation A which depends only upon the Hubbard-Stratonovich field. Typically, we are interested in Green's functions. For example, the estimator for the one-electron Green's function is

$$G_{ij\sigma}(\tau_{\ell}, (S)) = \frac{1}{1 + B_M^{\sigma} B_{M-1}^{\sigma} \cdots B_1^{\sigma}} B_{\ell}^{\sigma} B_{\ell-1}^{\sigma} \cdots B_1^{\sigma} \quad (10)$$

and

$$G_{ij\sigma}(\tau_{\ell}) = \sum_{\{S\}} G_{ij}(T_{\ell}, (S)) \frac{\det M_{\uparrow}(S) \det M_{\downarrow}(S)}{Z} \quad (11)$$

The calculations of various susceptibilities and multiparticle Green's functions are straightforward since once the Hubbard-Stratonovich transformation is introduced, one has a Wick theorem for the fermion operators. The only thing that one needs to remember is that disconnected diagrams must be retained because they can become connected by the subsequent average over the $S_i(\tau_{\ell})$ field.

In computing the product of the B matrices, one must be careful to control round-off errors as the number of products becomes large at low temperatures or at large U where $\Delta\tau$ must be small. In addition, there can be problems inverting the ill-conditioned sum of the unit matrix I and the product of the B matrices needed in Eqs. (8) and (10). Fortunately, a matrix stabilization procedure [16] overcomes these difficulties.

For the half-filled case ($\mu = 0$), provided there is only a near-neighbor hopping, H is invariant under the particle-hole transformation $c_{i\downarrow} = (-1)^i c_{i\downarrow}^{\dagger}$. Under this transformation, the last term in Eq. (6) for $\sigma = -1$ becomes

$$-\lambda \sum_i S_i(\tau_{\ell}) (1 - n_{i\downarrow}) \quad (12)$$

so that

$$\det M_{\downarrow}(S) = \prod_{i\ell} e^{\lambda \Delta\tau S_i(\tau_{\ell})} \det M_{\uparrow}(S) \quad (13)$$

This means that $\det M_\uparrow(S) \det M_\downarrow(S)$ is positive definite. In this case, the sum over the Hubbard-Stratonovich configurations can be done by Monte Carlo importance sampling, with the probability of a particular configuration $\{S(\tau_\ell)\}$ given by

$$P(S) = \frac{\det M_\uparrow(S) \det M_\downarrow(S)}{Z}. \quad (14)$$

Given M -independent configurations, selected according to the probability distribution Eq. 14, the expectation value of A is

$$\langle A \rangle = \frac{1}{M} \sum_{\{S\}} A(S). \quad (15)$$

When the system is doped away from half-filling, the product $\det M_\uparrow(S) \det M_\downarrow(S)$ can become negative. This is the so-called “fermion sign problem”. In this case, one must use the absolute value of the product of determinants to have a positive definite probability distribution for the Hubbard-Stratonovich configurations.

$$P_\parallel(S) = \frac{|\det M_\uparrow(S) \det M_\downarrow(S)|}{\sum_{\{S\}} |\det M_\uparrow(S) \det M_\downarrow(S)|} \quad (16)$$

Then, in order to obtain the correct results for physical observables, one must include the sign of the product of determinants [47]

$$s = \text{Sgn}(\det M_\uparrow(S) \det M_\downarrow(S)) \quad (17)$$

in the measurement

$$\langle A \rangle = \frac{\langle As \rangle_\parallel}{\langle s \rangle_\parallel}. \quad (18)$$

The \parallel subscript denotes that the average is over configurations generated with the probability distribution P_\parallel given by Eq. (16). If the average sign $\langle s \rangle_\parallel$ becomes small, there will be large statistical fluctuations in the Monte Carlo results. For example, if $\langle s \rangle_\parallel = 0.1$, one would have to sample of order 10^2 times as many independent configurations in order to obtain the same statistical error as when $\langle s \rangle_\parallel = 1$. On general grounds, one expects that $\langle s \rangle_\parallel$ decreases exponentially as the temperature is lowered.

The average sign $\langle s \rangle_\parallel$ also decreases as U increases and makes it (exponentially) difficult to obtain results at low temperatures for U of order the bandwidth and dopings of interest. Figure 1 illustrates just how serious this problem is and why other methods are required.

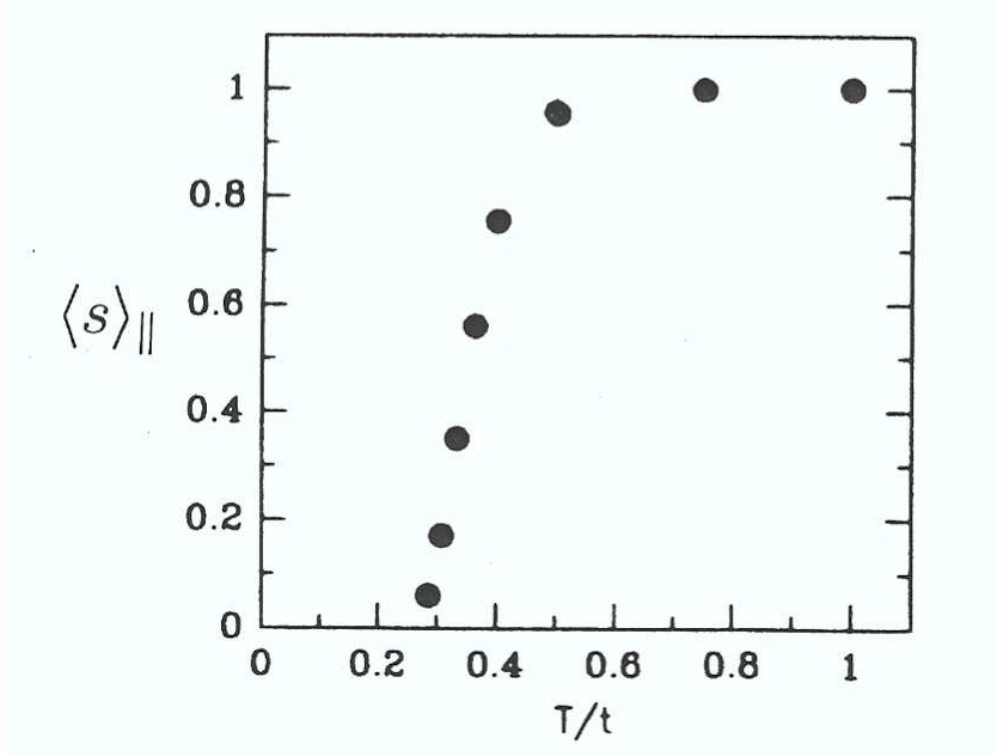


Figure 1: The average of the sign of the product of the fermion determinants, Eq. 17, that enters in the determinantal Monte Carlo calculations is shown versus temperature for an 8×8 lattice with $U = 8t$ and $\langle n \rangle = 0.87$. One can understand why calculations for $U = 8t$ with $T < 0.3$ become extremely difficult. (Scalapino [19])

The Dynamic Cluster Approximation

In the determinantal quantum Monte Carlo approach, one could imagine carrying out calculations on a set of $L \times L$ lattices and then scaling to the bulk thermodynamic limit. The dynamic cluster approximation [6] takes a different approach in which the bulk lattice is replaced by an effective cluster problem embedded in an external bath designed to represent the remaining degrees of freedom. In contrast to numerical studies of finite-sized systems in which the exact state of an $L \times L$ lattice is determined and then regarded as an approximation to the bulk thermodynamic result, the cluster theories give approximate results for the bulk thermodynamic limit. Then, as the number of cluster sites increases, the bulk thermodynamic result is approached.

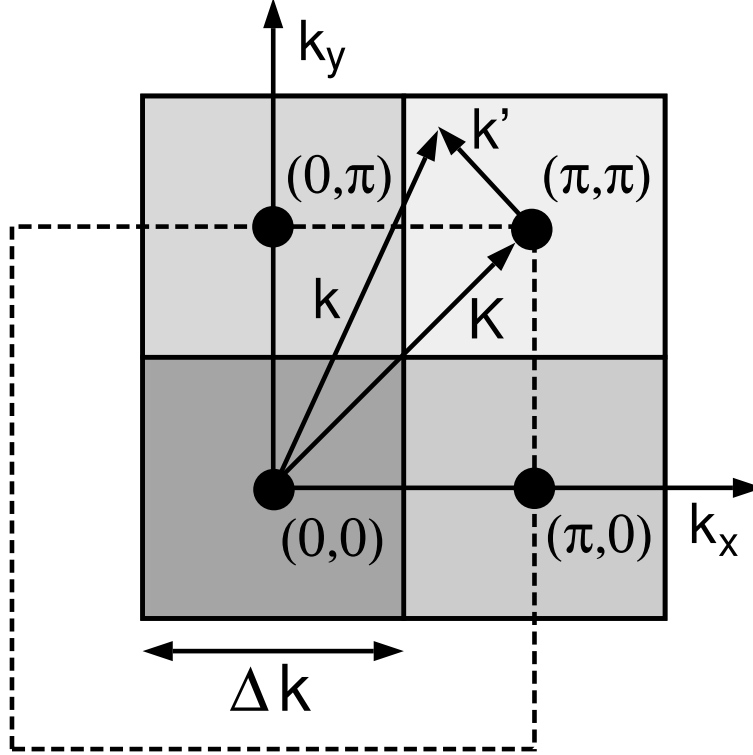


Figure 2: In the dynamic cluster approximation the Brillouin zone is divided into N_c cells each represented by a cluster momentum K . Then the self-energy and 4-point vertices are calculated on the cluster using an action determined by the inverse of the coarse-grained cluster-excluded propagator \mathcal{G}^{-1} , Eq. 21. This figure illustrates this coarse graining of the Brillouin zone for $N_c = 4$ (Maier *et al.* [6]).

In the dynamic cluster approximation, the Brillouin zone is divided into $N_c = L^2$ cells of size $(2\pi/L)^2$. As illustrated in Fig. 2, each cell is represented by a cluster momentum \mathbf{K} placed at the center of the cell. Then the self-energy $\Sigma(\mathbf{k}, \omega_n)$ is approximated by a coarse grained self-energy

$$\Sigma(\mathbf{K} + \mathbf{k}', \omega_n) \simeq \Sigma_c(\mathbf{K}, \omega_n) \quad (19)$$

for each \mathbf{k}' within the \mathbf{K}^{th} cell. The coarse grained Green's function is given by

$$\bar{G}(\mathbf{K}, \omega_n) \cong \frac{N_c}{N} \sum_{\mathbf{k}'} \frac{1}{i\omega_n - (\varepsilon_{\mathbf{K}+\mathbf{k}'} - \mu) - \Sigma_c(\mathbf{K}, \omega)} \quad (20)$$

where the lattice self-energy is replaced by the coarse grained self-energy. Given \bar{G} and Σ_c , one can set up a quantum Monte Carlo algorithm [6, 48] to calculate the cluster Green's

function. Here, the bulk lattice properties are encoded by using the cluster-excluded inverse Green's function

$$\mathcal{G}^{-1}(\mathbf{K}, \omega_n) = \bar{G}^{-1}(\mathbf{K}, \omega_n) + \Sigma_c(\mathbf{K}, \omega_n) \quad (21)$$

to set up the bilinear part of the cluster action. In Eq. (21), the cluster self-energy has been removed from \mathcal{G} to avoid double counting.

Then, the interaction on the cluster

$$\frac{U}{N_c} \sum_{\mathbf{K}, \mathbf{K}', \mathbf{Q}} c_{\mathbf{K}+\mathbf{Q}\uparrow}^\dagger c_{\mathbf{K}\uparrow} c_{\mathbf{K}'-\mathbf{Q}\downarrow}^\dagger c_{\mathbf{K}'\downarrow} \quad (22)$$

is linearized by introducing a discrete τ -dependent Hubbard-Stratonovich field on each τ -slice and for each \mathbf{K} point. In this way, the cluster problem is transformed into a problem of non-interacting electrons coupled to τ -dependent Hubbard-Stratonovich fields. Integrating out the bilinear fermion field and using importance sampling to sum over the Hubbard-Stratonovich fields one evaluates the cluster Green's function $G_c(\mathbf{K}, \omega_n)$. From this, one evaluates the cluster self-energy

$$\Sigma_c(\mathbf{K}, \omega_n) = \mathcal{G}^{-1}(\mathbf{K}, \omega_n) - G_c^{-1}(\mathbf{K}, \omega_n). \quad (23)$$

Then, using this new result for $\Sigma_c(\mathbf{K}, \omega_n)$ in Eq. 20, these steps are iterated to convergence.

Measurements of correlation functions and the 4-point vertex are made in the same manner as for the determinantal Monte Carlo. That is, after the Hubbard-Stratonovich field has been introduced, one has a Wick's theorem for decomposing products of various time-ordered operators. However, in this case there is an additional coarse-graining of the Green's function intermediate state legs [6, 42]. Since one is using a determinantal Monte Carlo method, there is also a sign problem for the doped Hubbard model. However, the self-consistent bath and the coarse-graining of the momentum space significantly reduce this problem so that lower temperatures can be reached. [49]

The Density Matrix Renormalization Group

The density-matrix-renormalization-group method was introduced by White. [44, 45] Here, as illustrated in Fig. 3 for a one-dimensional chain of length L , the system under study is

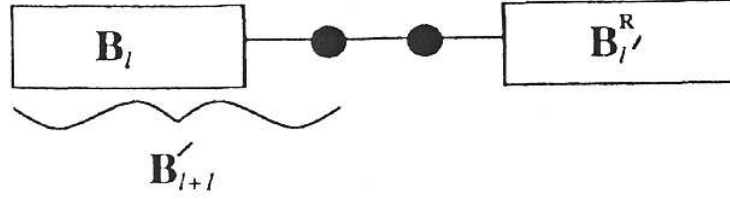


Figure 3: The configuration of blocks used for the density matrix renormalization group algorithm (White [45]).

separated into four pieces. A block B_ℓ containing $\ell = L/2 - 1$ sites on the left, a reflected $B_{\ell'}^R$ (right interchanged with left) block containing $\ell' = L/2 - 1$ sites on the right, and two additional sites in the middle. The left hand block B_ℓ and its near-neighbor site are taken to be the system to be studied, while the block $B_{\ell'}^R$ plus its adjacent site are considered to be the “environment”. The entire system is diagonalized using a Lanczos or Davidson algorithm to obtain the ground state eigenvalue and eigenvector ψ_o . Then, one constructs a reduced density matrix from ψ_o

$$\rho_{ii'} = \sum_j \psi_{oij}^* \psi_{oi'j}. \quad (24)$$

Here, $\psi_{oij} = \langle i | \langle j | \psi_o \rangle$ with $|i\rangle$ a basis state of the $\ell + 1$ block and $|j\rangle$ a basis state of the $\ell' + 1$ “environment” block. Then the reduced density matrix $\rho_{ii'}$ is diagonalized and m eigenvectors, corresponding to the m largest eigenvalues are kept. The Hamiltonian $H_{\ell+1}$ for the left hand block and its added site $B_{\ell+1}'$ is now transformed to a reduced basis consisting of the m leading eigenstates of $\rho_{ii'}$. The right hand environment block $H_{\ell'+1}^R$ is chosen to be a reflection of the system block including the added site. Finally, a superblock of size $L + 2$ is formed using $H_{\ell+1}$, $H_{\ell'+1}^R$ and two new single sites. Open boundary conditions are used. Typically, several hundred eigenstates of the reduced density matrix are kept and thus, although the system has grown by two sites at each iteration, the number of total states remains fixed and one is able to continue to diagonalize the superblock.

This infinite system method suffers because the groundstate wave function ψ_o continues to change as the lattice size increases. This can lead to convergence problems. Therefore,

in practice, a related algorithm in which the length L is fixed has been developed. In this case, instead of trying to converge to the infinite system fixed point under iteration, one has a variational convergence to the ground state of a finite system. This finite chain algorithm is similar to the one we have discussed but in this case the total length L is kept fixed and the separation point between the system and the environment is moved back and forth until convergence is achieved. [45, 5] Following this, one can consider scaling L to infinity.

In a sense, the density-matrix-renormalization-group method is a cluster theory. It embeds a numerical renormalization procedure in a larger lattice in which an exact diagonalization is carried out. The division of the chain into the system and the environment is similar in spirit to the embedded cluster and \mathcal{G}^{-1} . The use of the reduced density matrix, corresponding to the groundstate, to carry out the basis truncation provides an optimal focus on the low-lying states.

An important aspect of this approach is how rapidly the eigenvalues of the reduced density matrix fall off. This determines how many m states one needs to obtain accurate results. Unfortunately, for the study of n -leg Hubbard ladders, this fall-off becomes significantly slower as n increases and many more states must be kept. In addition, it appears that the behavior of the pairfield-pairfield correlation function is particularly sensitive to the number of states m that are kept. A measure of the errors associated with the truncation in the number m of density matrix eigenstates that are kept, is given by the discarded weight

$$W_m = \sum_{i=m+1}^D w_i. \quad (25)$$

Here, D is the dimension of the density matrix and w_i is its i^{th} eigenvalue. A useful approach is to increase m and extrapolate quantities to their values as $W_m \rightarrow 0$. The error in the groundstate eigenvalue varies as W_m and a typical extrapolation is shown in Fig. 4. For observables which do not commute with H , the errors vary as $\sqrt{W_m}$.

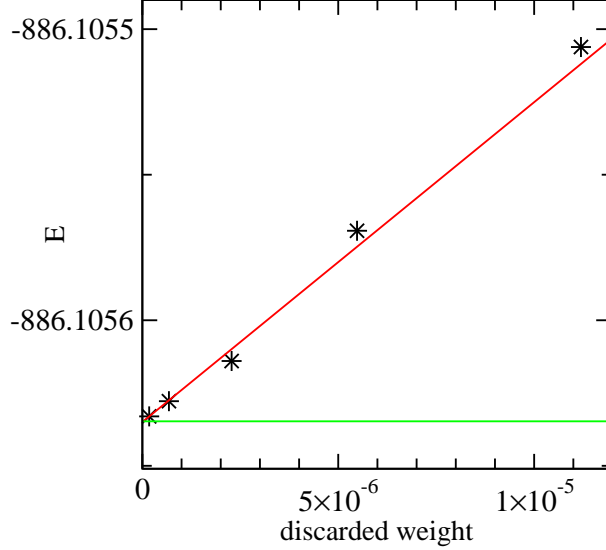


Figure 4: DMRG results for the ground state energy of a 2000-site Heisenberg spin-one-half chain versus the discarded weight W_m . The exact Bethe ansatz energy is shown as the line at the bottom of the figure. (S.R. White)

3. Properties of the 2D Hubbard Model

As we have discussed, the particle-hole symmetry of the half-filled Hubbard model with a near-neighbor hopping t leads to an absence of the fermion sign problem. In this case, the determinantal Monte Carlo algorithm [43] provides a powerful numerical tool for studying the low temperature properties of this model. In a seminal paper, Hirsch [15] presented numerical evidence that the groundstate of the half-filled two-dimensional Hubbard model with a near-neighbor hopping t and a repulsive on-site interaction $U > 0$ had long-range antiferromagnetic order. In this work, simulations on a set of $L \times L$ lattices were carried out. For each lattice, simulations were run at successively lower temperatures and extrapolated to the $T = 0$ limit. Then, a finite-size scaling analysis was used to extrapolate to the bulk $T = 0$ limit.

This work set the standard for what one would like to do in numerical studies of the Hubbard model. Unfortunately, the fermion sign problem prevents one from carrying out a similar determinantal Monte Carlo analysis for the doped case. However, various other

methods have been developed which provide information on the doped Hubbard model. Here, we will discuss results obtained from a dynamic cluster Monte Carlo algorithm. [6] This method also provides a systematic approach to the bulk limit as the cluster size increases. As noted in Sec. 2, the dynamic cluster Monte Carlo still suffers from the fermion sign problem, although to much less of a degree than the standard determinantal Monte Carlo. Maier *et al.* [27] have made the important step of studying the doped system on a sequence of different-sized clusters ranging up to 26 sites in size. Furthermore, this work recognized the importance of cluster geometry and developed a Betts'-like [50] grading scheme for determining which cluster geometries are the most useful in determining the finite-size scaling extrapolation.

Following this, we review a density-matrix-renormalization-group (DMRG) study [14] of a doped 6-leg Hubbard ladder in which the authors extrapolate their results to the limit of zero discarded weight and to legs of infinite length. This work provides evidence that static stripes exist in the ground state for large values of U ($U \simeq 12t$) but are absent at weaker coupling ($U \lesssim 3t$). We conclude this section with a discussion of the pseudogap behavior which is observed in the lightly doped Hubbard model when U is of order the bandwidth.

The Antiferromagnetic Phase

Determinantal quantum Monte Carlo results for the equal-time magnetization-magnetization correlation function

$$C(\ell) = \langle m_{i+\ell}^z m_i^z \rangle \quad (26)$$

with $m_i^z = (n_{i\uparrow} - n_{i\downarrow})$ are plotted in Fig. 5. These results are for a half-filled Hubbard model on a 10×10 lattice at a temperature $T = 0.1t$ with $U = 4t$. At this temperature, the antiferromagnetic correlation length exceeds the lattice size and the cluster is essentially in its groundstate. Strong antiferromagnetic correlations are clearly visible in $C(\ell)$.

The magnetic structure factor, shown in Fig. 6

$$S(q) = \frac{1}{N} \sum e^{-i\mathbf{q} \cdot \boldsymbol{\ell}} \langle m_{i+\boldsymbol{\ell}}^z m_i^z \rangle \quad (27)$$

has a peak at $q = (\pi, \pi)$ reflecting the antiferromagnetic correlations. As shown in Fig. 7, as the temperature is lowered $S(\pi, \pi)$ grows and then saturates when the antiferromagnetic

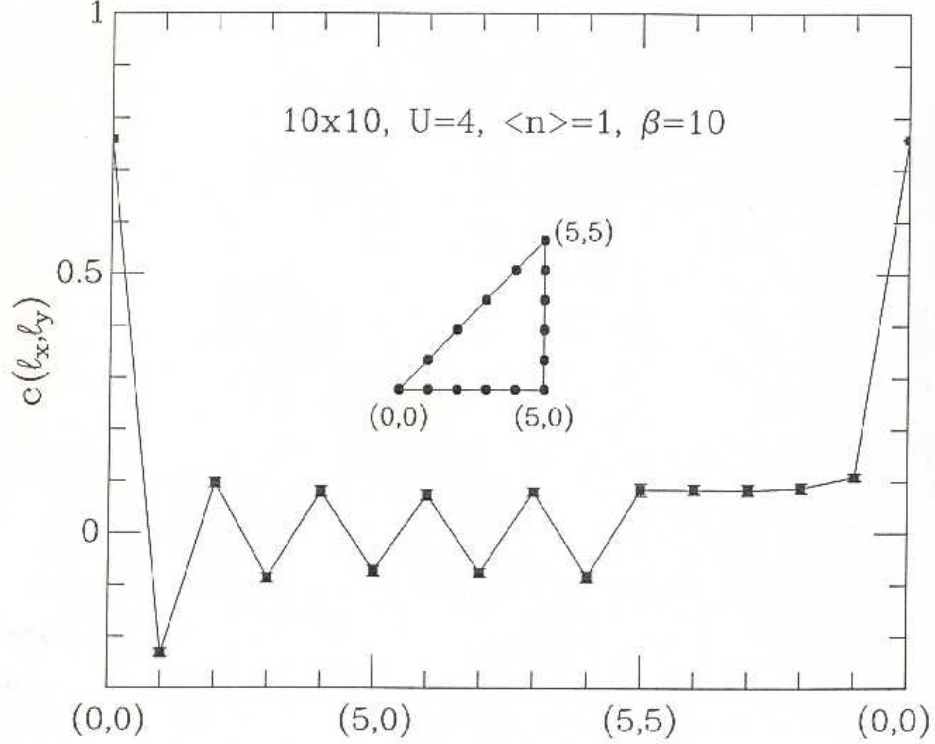


Figure 5: The equal-time magnetization-magnetization correlation function $C(\ell_x, \ell_y)$ on a 10×10 lattice with $U = 4t$, $\langle n \rangle = 1$ and $T = 0.1t$. The horizontal axis traces out the triangular path on the lattice shown in the inset. Strong antiferromagnetic correlations are seen (Hirsch [15], Moreo *et al.* [17]).

correlations extend across the lattice. If there is long-range antiferromagnetic order in the groundstate, the saturated value of $S(\pi, \pi)$ will scale with the number of lattice sites $N = L \times L$. Furthermore, based upon spin-wave fluctuations, [51] one expects that the leading correction will vary as $N^{\frac{1}{2}}$ so that

$$\lim_{N \rightarrow \infty} \frac{S(\pi, \pi)}{N} = \frac{\langle m_x \rangle^2}{3} + \frac{A}{N^{\frac{1}{2}}}. \quad (28)$$

Fig. 8 shows $S(\pi, \pi)/N$ versus $N^{-\frac{1}{2}}$ for $U = 4t$ and one sees that the groundstate has long-range antiferromagnetic order. In his original paper, Hirsch [15] concluded that the groundstate of the half-filled 2D Hubbard model with a near-neighbor hopping t would have long-range antiferromagnetic order for $U > 0$.

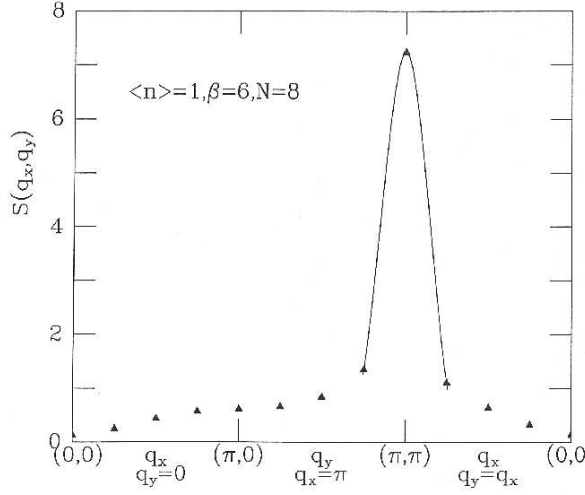


Figure 6: $S(q_x, q_y)$ versus q_x, q_y for $\langle n \rangle = 1$, $U = 4t$ and $T = .167t$. The solid line is a fit to guide the eye (Hirsch [15], Moreo *et al.* [17]).

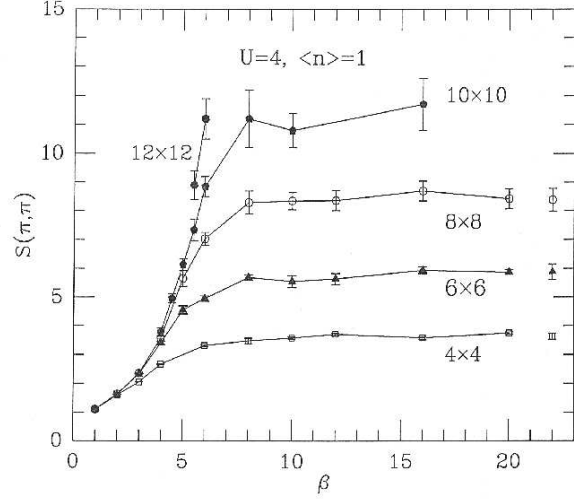


Figure 7: The antiferromagnetic structure factor $S(\pi, \pi)$ for $\langle n \rangle = 1$ and $U = 4$ as a function of the inverse temperature β for various lattice sizes. $S(\pi, \pi)$ saturates when the coherence length exceeds the lattice size (Hirsch [15], White *et al.* [16]).

$d_{x^2-y^2}$ Pairing

The structure of the pairing correlations in the doped 2D Hubbard model were initially studied using the determinantal Monte Carlo method. The d-wave pairfield susceptibility

$$P_d = \int_0^\beta d\tau \langle \Delta_d(\tau) \Delta_d^\dagger(0) \rangle \quad (29)$$

with

$$\Delta_d^\dagger = \frac{1}{2\sqrt{N}} \sum_{\ell, \delta} (-1)^\delta c_{\ell\uparrow}^\dagger c_{\ell+\delta\downarrow}^\dagger \quad (30)$$

was calculated. Here δ sums over the four near-neighbor sites of ℓ and $(-1)^\delta$ gives the $+-+-$ sign alteration characteristic of d-wave pairing. The doped Hubbard model has a fermion sign problem, so that the Hubbard-Stratonovich fields must be generated according to the probability distribution $P_\parallel(S)$ given by Eq. (16). In this case, it is essential to include the sign factor s in the evaluation of observables. The (red) circles in Fig. 9 show results [47] for $P_d(T)$ obtained on a 4×4 lattice with $\langle n \rangle = 0.875$ and $U = 4t$. If the sign s is not

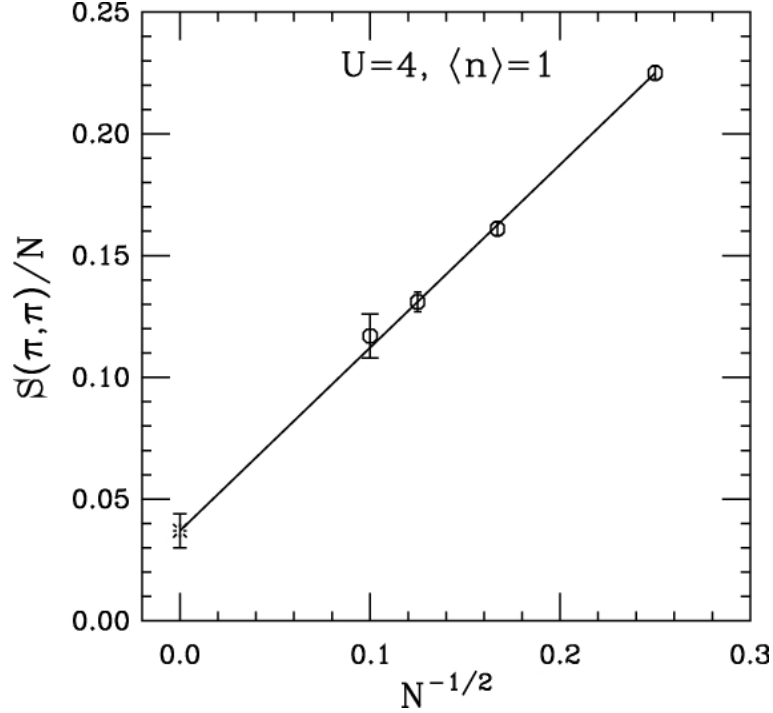


Figure 8: The zero-temperature limit of $S(\pi, \pi)/N$ versus $1/N^{1/2}$. The results extrapolate to a finite value as $N \rightarrow \infty$ implying that there is long range antiferromagnetic order in the groundstate of the infinite lattice (Hirsch [15], White *et al.* [16]).

included, one obtains the (blue) squares. The neglect of this sign in early work [52] left the false impression that the Hubbard model did not support $d_{x^2-y^2}$ pairing.

As seen, when the sign is included, the d-wave pairfield susceptibility increases as the temperature is lowered. However, over the temperature range accessible to the determinantal Monte Carlo, it remains smaller than the $U = 0$ result P_{do} , shown as the (blue) dashed line in Fig. 10. In Ref. [16], it was argued that this behavior was due to the renormalization of the single particle spectral weight and that the significant feature to note was that $P_d(T)$ was enhanced over

$$\overline{P}_d(T) = \frac{T}{N} \sum_{pn} G(p) G(-p) (\cos p_x - \cos p_y)^2. \quad (31)$$

Here, $G(p)$ is the dressed single particle Green's function determined from the Monte Carlo simulation and \overline{P}_d corresponds to the contribution of a pair of dressed but non-interacting

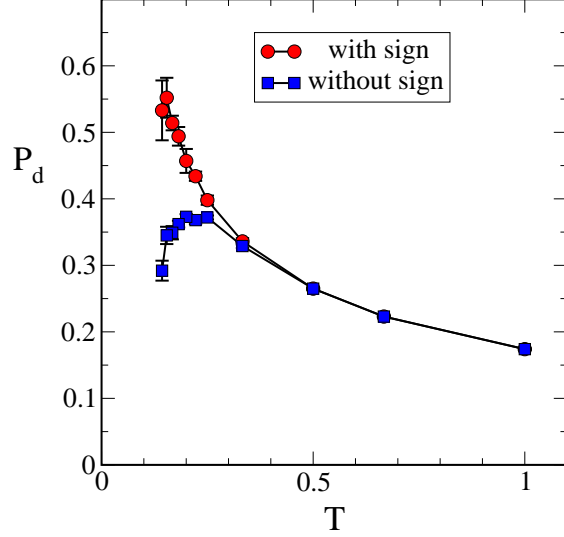


Figure 9: The d-wave pairfield susceptibility $P_d(T)$ (red circles) for a 4×4 lattice with $U = 4t$ and $\langle n \rangle = 0.875$ versus temperature T measured in units of the hopping t . The (blue squares) show the erroneous result that is found if the fermion sign is ignored. (Loh *et al.* [47])

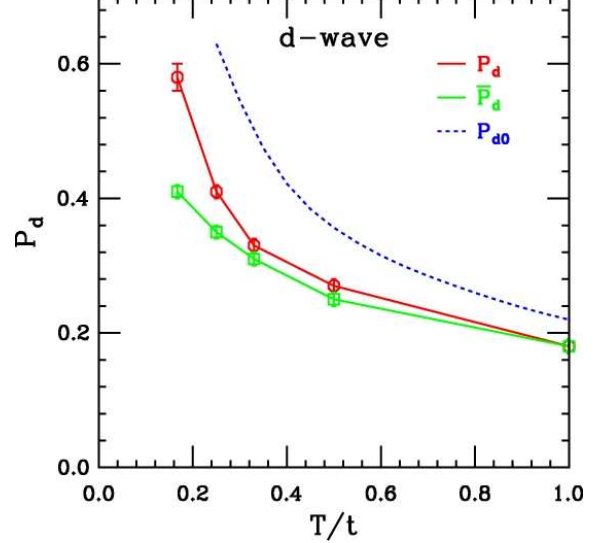


Figure 10: The d-wave pair-field susceptibility $P_d(T)$ is shown as the open (red) circles. The open (green) squares show results for the “noninteracting” pair-field susceptibility $\bar{P}_d(T)$ calculated using dressed single-particle Green’s functions, Eq. 31, while the dashed (blue) curve is the noninteracting susceptibility P_{d0} calculated with the bare Green’s functions. (White *et al.* [16])

holes. The fact that $\bar{P}_d(T)$ lies below $P_d(T)$ implies that there is an attractive $d_{x^2-y^2}$ -pairing interaction between the holes. $\bar{P}_d(T)$ is shown as the (green) curve labeled with open squares in Fig. 10.

In order to determine what happens at lower temperatures, Maier *et al.* [27] have determined $P_d(T)$ using a dynamic cluster approximation. In a systematic study, they provided evidence that the doped Hubbard model contained a $d_{x^2-y^2}$ pairing phase. In this work, the authors adapted a cluster selection criteria originally introduced by Betts *et al.* [50] in a numerical study of the 2D Heisenberg model. For the Heisenberg model, Betts *et al.* [50] showed that an important selection criteria for a cluster was the completeness of the “al-

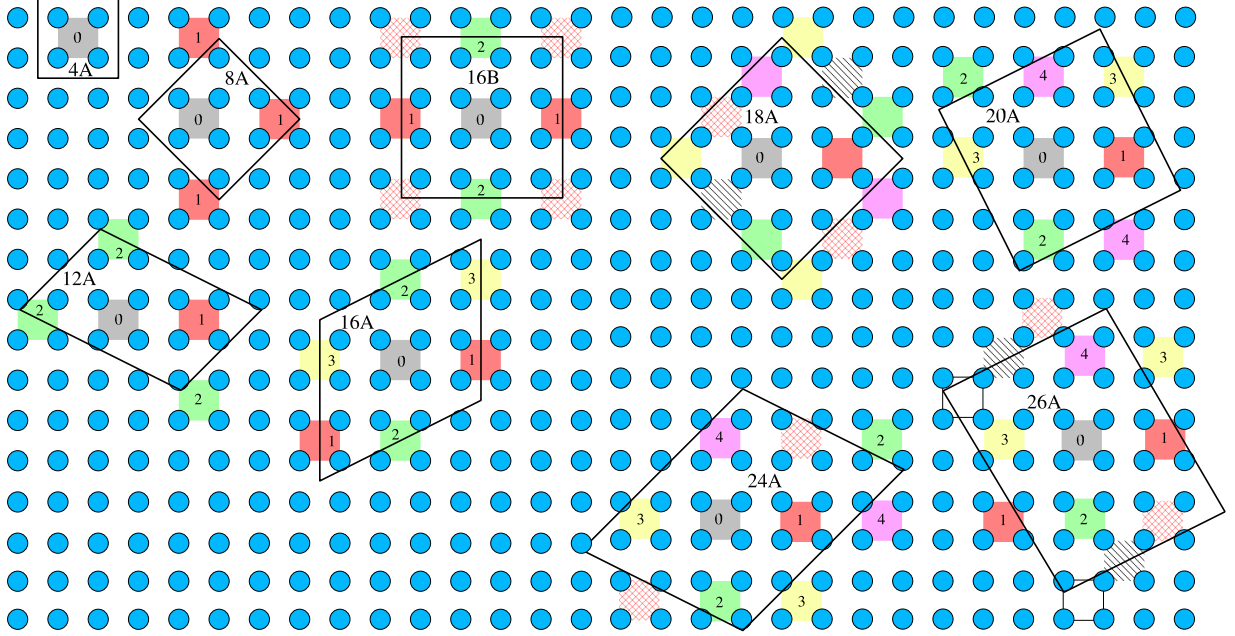


Figure 11: Cluster sizes and geometries used by Maier *et al.* [27] in their study of the d-wave pair-field susceptibility. The shaded squares represent independent d-wave plaquettes within the clusters. In small clusters, the number of neighboring d-wave plaquettes Z_d listed in Table 1 is smaller than 4, i.e., than that for an infinite lattice. (Maier *et al.* [27])

lowed neighbor shells” compared to an infinite lattice. They found that a finite-size scaling analysis was greatly improved when clusters with the most complete shells were selected. For a d-wave order parameter, Maier *et al.* noted that one needs to take into account the non-local 4-site plaquette structure of the order parameter in applying this criteria. As illustrated in Fig. 11, the 4-site cluster encloses just one d-wave plaquette. Denoting the number of independent near-neighbor plaquettes on a given cluster by Z_d , the 4-site cluster has no near-neighbors so that $Z_d=0$. In this case the embedding action does not contain any pair field fluctuations and hence T_c is over estimated. Alternatively, the 8A cluster has space for one more 4-site plaquette ($Z_d = 1$) and the same neighboring plaquette is adjacent to its partner on all four sides. In this case the phase fluctuations are over estimated and T_c is suppressed. For the 16B cluster, one has $Z_d = 2$ while $Z_d = 3$ for the oblique 16A cluster. Thus, one expects that the pairing correlations for the 16B cluster will be suppressed relative

to those for the 16A cluster. The number of independent neighboring d-wave plaquettes Z_d for the clusters shown in Fig. 11 are listed in Table 1.

Cluster	Z_d	T_c/t
4	0 (MF)	0.056
8A	1	-0.006
18A	1	-0.022
12A	2	0.016
16B	2	0.015
16A	3	0.025
20A	4	0.022
24A	4	0.020
26A	4	0.023

Table 1: Number of independent neighboring d-wave plaquettes Z_d and the value T_c obtained from a linear fit of the pair-field susceptibility in Fig. 12 (Maier *et al.* [27]).

Results for the inverse of the pair field susceptibility versus T for $U = 4t$ and $\langle n \rangle = 0.9$ are shown in Fig. 12. As expected, the 4-site cluster results over estimate T_c and the results for the 8A and 18A clusters do not give a positive value for T_c . However, successive $Z_d = 4$ results on larger lattices fall nearly on the same curve. These results suggest that the 2D Hubbard model with $U = 4t$ and $\langle n \rangle = 0.9$ has a $d_{x^2-y^2}$ pairing phase. The dynamic cluster approximation leads to a mean field behavior close to T_c . [53] Values of T_c obtained using a mean field linear fit of the low temperature data for the various clusters are listed in Table 1.

If $T_c \simeq .02t$ and we take $t = 0.2$ eV, this gives $T_c \sim 50K$. We believe that T_c will increase with U , reaching a maximum when U is of order the bandwidth. In addition, we expect that the transition temperature is sensitive to the one-electron tight binding parameters. An example which illustrates this is known from density matrix renormalization-group calculations for the 2-leg Hubbard ladder. [54] Figure 13 shows an average of the rung-rung pairfield correlations

$$\overline{D} = \sum_{\ell} \langle \Delta(i + \ell) \Delta^{\dagger}(i) \rangle \quad (32)$$

for a 2×16 Hubbard ladder versus the ratio of the rung to leg hopping parameters t_{\perp}/t .

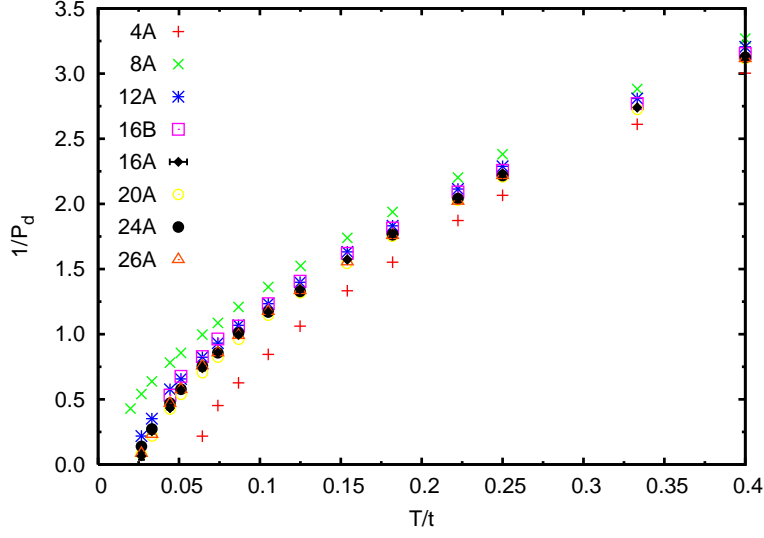


Figure 12: The inverse of the d-wave pair-field susceptibility is plotted versus T/t for various clusters. Here $U = 4t$ and $\langle n \rangle = 0.9$. (Maier *et al.* [27])

Here

$$\Delta^\dagger(i) = c_{i1\uparrow}^\dagger c_{i2\downarrow}^\dagger - c_{i1\downarrow}^\dagger c_{i2\uparrow}^\dagger \quad (33)$$

creates a pair on the i^{th} rung of the ladder. The pairing, as measured by \overline{D} exhibits a maximum at a value of t_\perp/t when the minimum of the antibonding band at $k_x = 0$ and the maximum of the bonding band at $k_x = \pi$ approach the fermi surface. For the half-filled noninteracting system, this would occur when $t_\perp/t = 2$. The doping and the interaction U leads to a reduction of this ratio and to a flattening of the dispersion which further enhances the single particle spectral weight near the fermi energy. If one considers the antibonding band to have $k_y = \pi$ and the bonding band to have $k_y = 0$, then this behavior is similar to increasing the single-particle spectral weight near $(0, \pi)$ and $(\pi, 0)$ in the 2D Hubbard model. One also sees that the largest peak in \overline{D} occurs when U is of order the bandwidth.

Having argued that the bandstructure plays a key role in determining T_c , it is important to note that this raises a puzzle. State of the art LDA calculations, as Andersen and coworkers have shown, [55] can be folded down to give material specific near-neighbor t , next-near-neighbor t' , etc. hopping parameters. For the one-band Hubbard model one would then

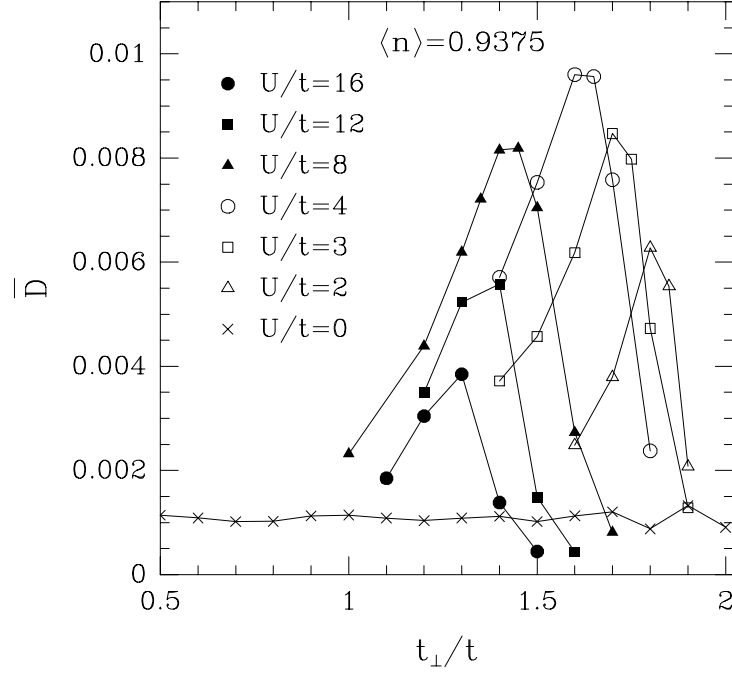


Figure 13: \bar{D} versus t_{\perp}/t for various values of U/t at a filling $\langle n \rangle = 0.9375$ (Noack *et al.* [54]).

have for the one-electron energy

$$\mathcal{E}_k = -2t(\cos k_x + \cos k_y) - 4t' \cos k_x \cos k_y - \dots \quad (34)$$

From an analysis of a large number of hole-doped cuprates, it was found that T_c is correlated with the range of the intra-layer hopping. [56] For the one-band Hubbard model that we have discussed, this analysis implies that T_c should increase as t'/t becomes more negative. The opposite trend is seen in both dynamic cluster [57] and density matrix renormalization-group calculations. [13, 58] However, a projected fermion calculation [59] finds that t' enters the effective interaction and can lead to an increase in T_c which is consistent with the conclusions of Ref. [56]. The resolution of this puzzle represents an important open problem.

Stripes

In a DMRG study of 7×6 Hubbard ladders with 4r holes, Hager *et al.* [14] found that the ground state was striped for strong coupling values of U ($U = 12t$). Using a systematic extrapolation they gave evidence that such stripes exist in infinitely long 6-leg ladders. These studies also found that for small values of U ($U = 3t$) there were no stripes in the ground state. This work extended earlier work [60] on a 7×6 system with 4 holes which found that a well-defined stripe formed for $U/t \sim 8$ to 12. The absence of stripes for weak coupling is consistent with the fact that weak coupling renormalization group studies of the Hubbard model find no evidence of a stripe instability. [36, 37]

Using the DMRG technique, the ground state expectation values of the hole-density

$$h(x) = \sum_{y=1}^6 (1 - \langle n(x, y) \rangle) \quad (35)$$

and the staggered spin density

$$s(x) = \sum_{y=1}^6 (-1)^{x+y} \langle n_{\uparrow}(x, y) - n_{\downarrow}(x, y) \rangle \quad (36)$$

were evaluated for 7×6 ladders with 4r holes. Periodic boundary conditions were used for the 6-site direction and open boundaries were used in the leg direction. Results for the hole $h(x)$ and spin $s(x)$ densities for a 21×6 ladder doped with 12 holes are shown in Fig. 14. One sees from the modulation of the hole density along the leg direction that three stripes have formed. These stripes, each associated with 4 holes, run around the 6-site cylinder. In earlier t-J studies, [12] a preferred stripe density of half-filling was found and we believe that the $2/3$ filling seen in Fig. 14 is a consequence of the restriction to 6 legs. Just as in the t-J ladder calculations, the staggered spin density undergoes a π -phase shift where the hole density is maximal. The finite staggered spin density is an artifact of the DMRG procedure in which no spin symmetry was imposed. This, along with the open boundary conditions which break the translational symmetry allow the charge and spin density structures to appear in the $h(x)$ and $s(x)$ expectation values.

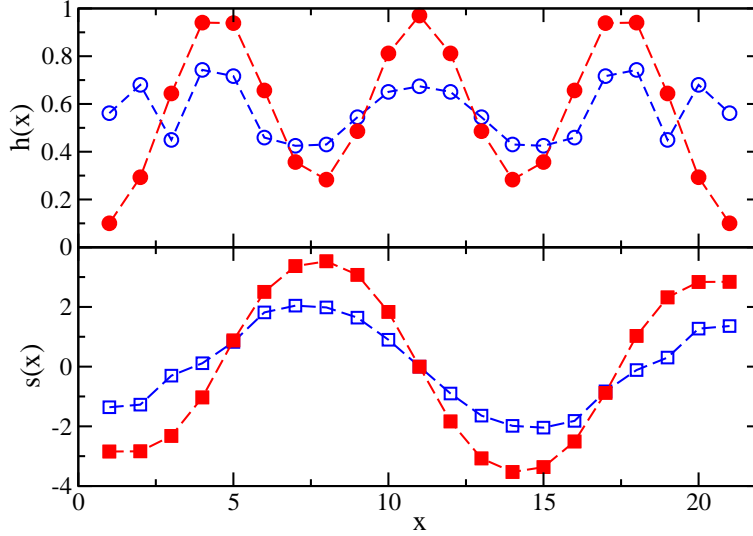


Figure 14: The hole $h(x)$ (circle) and staggered spin $s(x)$ (square) densities in the leg x -direction are plotted for a 21×6 ladder with 12 holes for $U = 12t$ (solid symbols) and $U = 3t$ (open symbols). (Hager *et al.* [14])

While stripe-like structures are seen in Fig. 14 for both $U/t = 12$ and $U/t = 3$, the amplitude of the charge density modulations for $U/t = 3$ are both smaller and less regular than the $U/t = 12$ results. As discussed in Sec. 2, DMRG results for operators which are non-diagonal in the energy basis are expected to deviate from their exact values by the square root of the discarded weight $\sqrt{W_m}$ as the number of basis states is increased. Thus, to determine whether there are stripes in the ground state of an infinite ladder, Hager *et al.* [14] extrapolated their results for a set of $7r \times 6$ ladders to $W_m \rightarrow 0$ and then took $R = 7r \rightarrow \infty$. They did this for the wave-vector power spectrum of the charge density

$$H^2 = \sum_{k_x} |H(k_x)|^2 \quad (37)$$

with

$$H(k_x) = \sqrt{\frac{2}{R+1}} \sum_x \sin(k_x x) \langle h(x) \rangle. \quad (38)$$

For a ladder with a periodic array of stripes separated by 7 sites, the maximum contribution to H^2 is associated with the wave vector

$$\frac{k_x^*}{\pi} = \frac{2r+1}{R+1} \rightarrow \frac{2}{7} \quad (39)$$

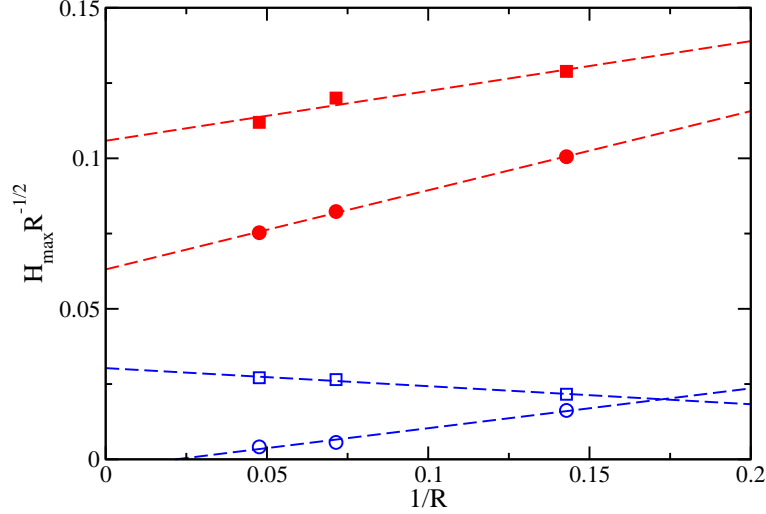


Figure 15: The amplitude of the power spectrum component $|H(k_x^*)|/\sqrt{R}$ for the hole density modulation. Results for a fixed number ($6000 \leq m \leq 8000$) of density-matrix eigenstates (squares) and results extrapolated to the limit $W_m \rightarrow 0$ (circles) are shown as a function of the inverse ladder length $1/R$ for $U = 12t$ (solid symbols) and $U = 3t$ (open symbols). The dashed lines are linear fits. (Hager *et al.* [14])

and

$$H_{\max} = |H(k_x^*)| \propto \sqrt{R} h_0 \quad (40)$$

as R goes to infinity. In Fig. 15, the amplitude $H_{\max}(k_x^*)/\sqrt{R}$ is plotted for $U/t = 12$ and $U/t = 3$ versus the inverse of the ladder length R^{-1} . The solid squares show the results when a fixed number ($6000 \leq m \leq 8000$) of density-matrix eigenstates are retained. The solid circles are the extrapolated $W_m \rightarrow 0$ ($m \rightarrow \infty$) results for $U/t = 12$. Similar results are shown using open symbols for $U/t = 3$. When the $W_m \rightarrow 0$ results are then extrapolated to $R \rightarrow \infty$, one sees clear evidence for stripes when $U/t = 12$ and an absence of stripes for $U/t = 3$. Note the importance of the $W_m \rightarrow 0$ extrapolation in determining the absence of stripes for $U/t = 3$.

The Pseudogap

Besides the antiferromagnetic, d-wave pairing, and striped phases, the cuprates exhibit a normal state pseudogap below a characteristic temperature T^* when they are underdoped.

This pseudogap manifests itself in a variety of ways. [61] There is a decrease in the Knight shift, reflecting a decrease in the magnetic susceptibility. [62] This was interpreted in terms of the opening of a pseudogap in the spin degrees of freedom. Observations of a similar suppression in the tunneling density of states, [63] the c-axis optical conductivity [64] and the specific heat [65] made it clear that there was a pseudogap in both the spin and charge degrees of freedom. ARPES studies show that in the hole-doped materials, a pseudogap opens near the $(\pi, 0)$ antinodal regions while in the electron-doped materials, at the lowest dopings, it opens along the nodal direction near $(\frac{\pi}{2}, \frac{\pi}{2})$. [66] The pseudogap appears in the underdoped region of the phase diagram and weakens as optimal doping is approached. If the Hubbard model is to contain the essential physics of the cuprates, it should exhibit the pseudogap phenomenon.

Before looking for evidence of pseudogap behavior in the doped Hubbard model, it is useful to first look at the structure of the single particle spectral weight for the half-filled Hubbard model. An important paper on this was that of Preuss *et al.* [20] Here, determinantal Monte Carlo calculations of the finite temperature single particle Green's function $G(k, \tau)$ were carried out on an 8×8 periodic lattice. The spectral weight

$$A(k, \omega) = -\frac{1}{\pi} \text{Im} G(k, i\omega_n \rightarrow \omega + i\delta) \quad (41)$$

was then determined using a numerical maximum entropy continuation. Results for the half-filled case with $U = 8t$ and $T = 0.1t$ are shown in Fig. 16a. Here, $A(k, \omega)$ is plotted versus ω for various k values in the Brillouin zone. Figure 16b summarizes these results using a standard “band structure” ω versus k plot in which the dark areas signify a large spectral weight. This work and related studies [67] showed that when U was of order the bandwidth or larger, there were four bands consisting of two incoherent upper and lower Hubbard bands and two quasiparticle-like, narrow bands nearer $\omega = 0$. The inner bands were found to have a dispersion set by $J \cong 4t^2/U$ while the outer, upper and lower Hubbard bands, appear as an essentially dispersionless incoherent background.

The left hand part of Fig. 17 shows the single particle density of states for the half-filled case. Here, when the temperature is small compared to the exchange energy $J \sim 4t^2/U$, one

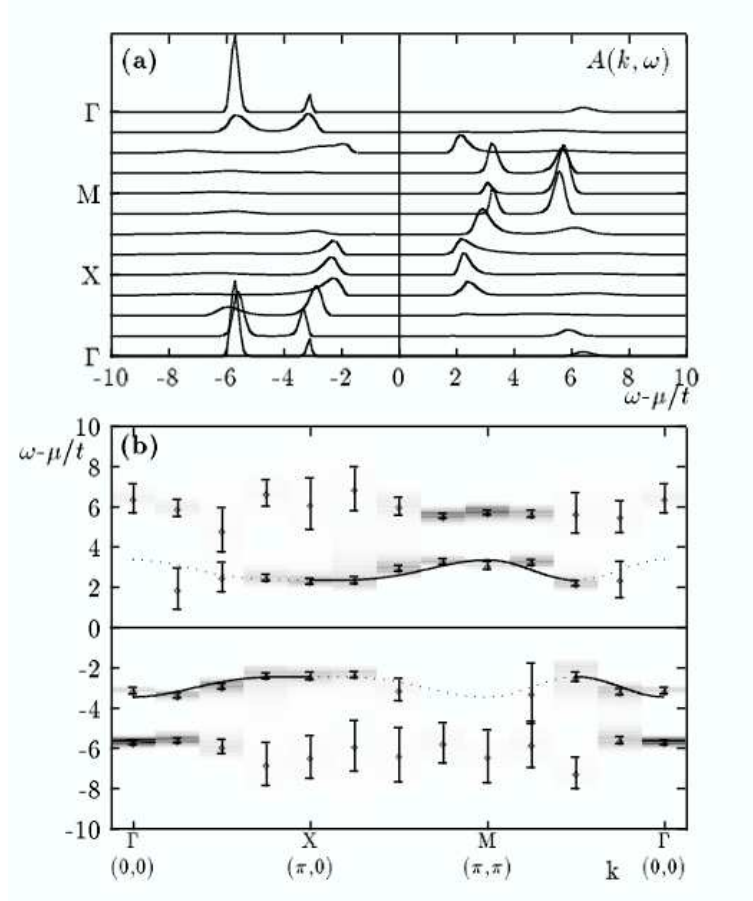


Figure 16: Single-particle spectral weight $A(k, \omega)$ for an 8×8 Hubbard model at half-filling $\langle n \rangle = 1$ with $U = 8t$ and $T = 0.1t$. (a) $A(k, \omega)$ versus ω for different values of k and (b) ω versus k plotted as a “band-structure” where sizable structure in $A(k, \omega)$ is represented by the strongly shaded regions and peaks by error bars. (Preuss *et al.* [20])

clearly sees the broad upper and lower Hubbard bands and the narrow inner bands. When the system is hole-doped, the chemical potential moves down into the narrow coherent band that lays below $\omega = 0$ for the half-filled case and at the same time the upper coherent band loses weight and disappears as shown on the right hand side of Fig. 17. This is also seen in Fig. 18 which shows $A(k, \omega)$ for $\langle n \rangle = .95$ from Ref. [20]. Here, one sees that the dispersing band below $\omega = 0$ in the insulator and the band that the holes are doped into as the system becomes metallic are quite similar. At the same time, the narrow dispersing band that lays just above $\omega = 0$ in the insulating state has lost most of its spectral weight.

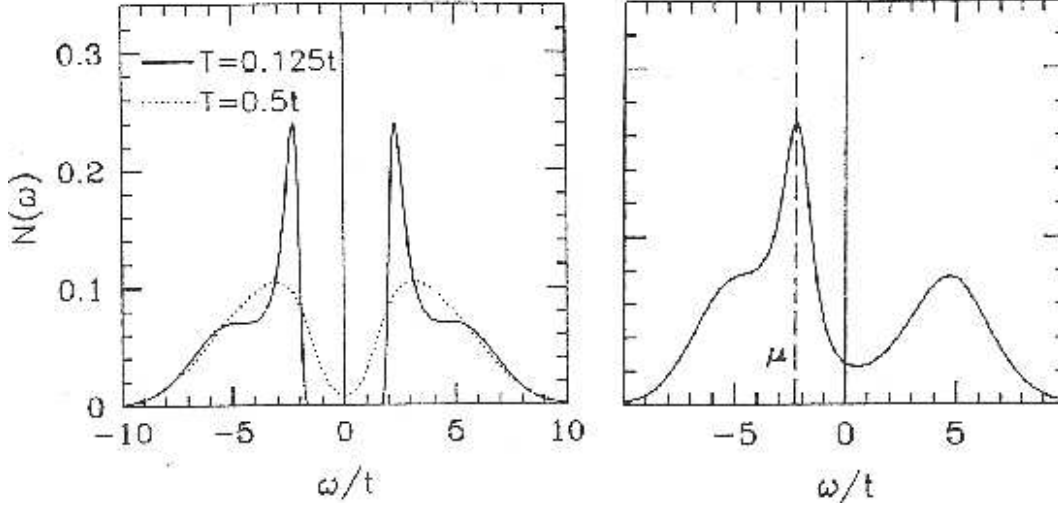


Figure 17: On the left, the single particle density of states $N(\omega)$ versus ω for $U = 8t$ and $\langle n \rangle = 1$. On the right, $N(\omega)$ for the hole doped $\langle n \rangle = 0.875$, $U = 8t$ case at $T = 0.33t$ (Scalapino [68]).

For the doped system, the fermion sign problem limited the temperature to $T = t/3$ for the determinantal data shown in Fig. 18, but later similar determinantal Quantum Monte Carlo runs at $T = 0.25t$ and a filling of 0.95 found evidence for the formation of a pseudogap near $(\pi, 0)$. [21] In this work, the spin susceptibility was shown to have a large spectral weight at well defined spin excitations for the doping and temperature range in which the pseudogap appeared. There was no pseudogap in the overdoped $\langle n \rangle \lesssim 0.8$ regions where the spectral weight of the spin susceptibility became broad and featureless.

Dynamic cluster Monte Carlo calculations [28] with $U = 6t$ and $\langle n \rangle = 0.95$ find that the magnetic spin susceptibility exhibits a clear decrease below a temperature $T \cong 0.1t$, as shown in the inset of Fig. 19 and simulations at $T = .06t$ gave the results for $A(k, \omega)$ shown in Fig. 19. Here, a pseudogap has opened for $k = (\pi, 0)$, while the nodal region with $k = (\frac{\pi}{2}, \frac{\pi}{2})$ remains gapless. In addition, a variety of other cluster calculations [7, 29, 30, 32] have found pseudogap behavior in both hole- and electron-doped Hubbard models and studied its dependence on the next near-neighbor hopping t' . The t' dependence as well as the doping dependence are consistent with renormalization-group calculations which show the importance of umklapp scattering processes [37] and the short range antiferromagnetic spin

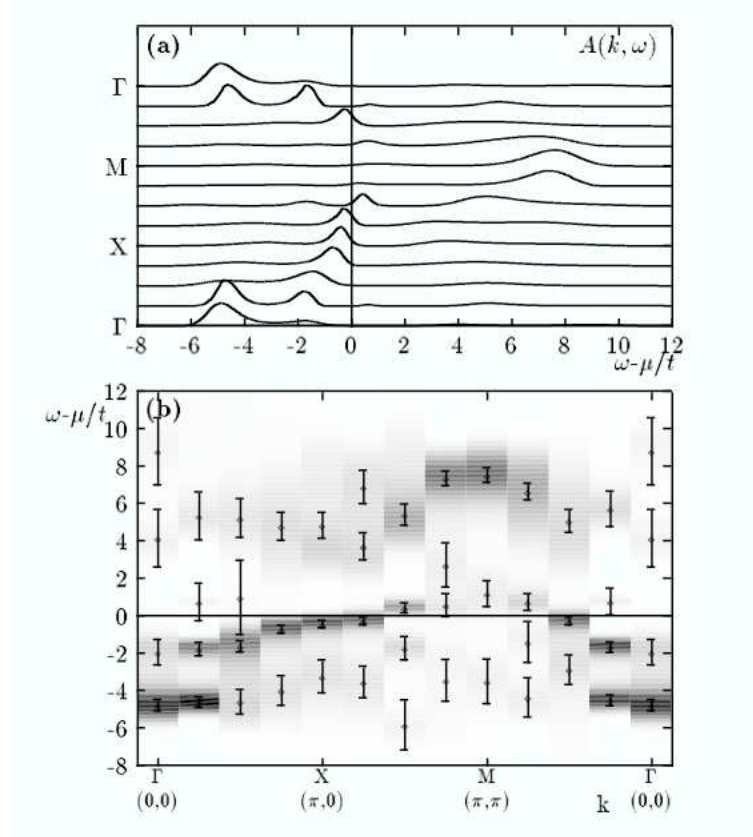


Figure 18: The single-particle spectral weight $A(k, \omega)$ for the hole doped $\langle n \rangle = 0.95$ system at a temperature $T = 0.33t$. This plot is similar to Fig. 16 and shows what happens as holes are doped into the Mott-Hubbard insulator. (Preuss *et al.* [20])

correlations.

In the next section, we turn to a discussion of the effective pairing interaction. Specifically, the structure of the two-particle irreducible vertex and its associated d-wave eigenfunction are analyzed.

4. The Structure of the Effective Pairing Interaction

As discussed in Section 3, determinantal quantum Monte Carlo studies of the doped two-dimensional Hubbard model find that $d_{x^2-y^2}$ pairing correlations develop as the temperature is lowered and a dynamic cluster quantum Monte Carlo calculation on Betts' clusters finds

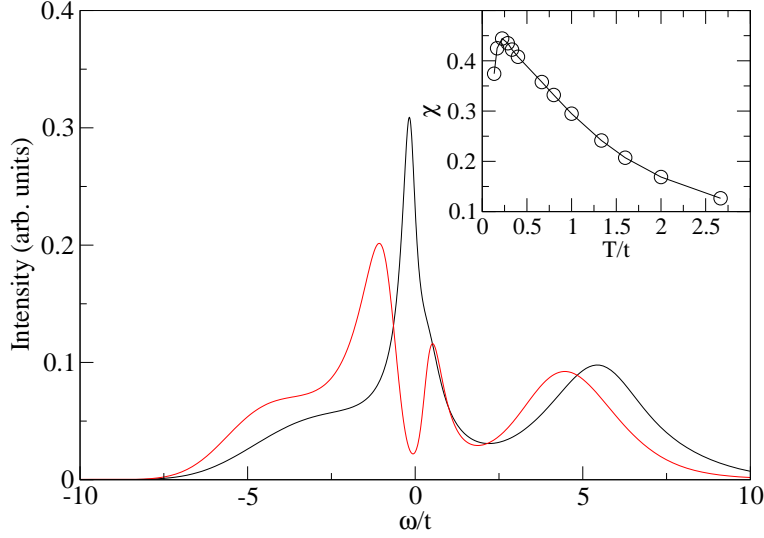


Figure 19: The single particle spectral weight $A(k, \omega)$ versus ω for the antinodal $k = (\pi, 0)$ (red curve) and nodal $k = (\pi/2, \pi/2)$ (black curve) momenta of an underdoped $\langle n \rangle = 0.95$, $U = 6t$ Hubbard model at $T = 0.11t$. The inset shows the temperature dependence of the magnetic susceptibility. (M. Jarrell)

evidence for a finite temperature d-wave superconducting phase. Here we discuss how one can use numerical techniques to determine the structure of the interaction responsible for the pairing. The basic idea is to numerically calculate the four-point vertex Γ and the single particle propagator G (solid lines) shown in Fig. 20. Then, using the particle-particle Bethe-Salpeter equation (Fig. 20a), one can extract the two-particle irreducible vertex Γ^{pp} which is the pairing interaction. As we will discuss, the four-point vertex Γ also contains information on the particle-hole magnetic ($S = 1$) and charge ($S = 0$) channels. Thus, it provides a natural framework for understanding the relationship of the pairing interaction to these other channels.

Using quantum Monte Carlo simulations, one can calculate both the one- and two-fermion Green's functions

$$G(x_2, x_1) = -\langle T c_{\sigma}(x_2) c_{\sigma}^{\dagger}(x_1) \rangle \quad (42)$$

and

$$G_2(x_4, x_3, x_2, x_1) = -\langle T c_{\sigma_4}(x_4) c_{\sigma_3}(x_3) c_{\sigma_2}^{\dagger}(x_2) c_{\sigma_1}^{\dagger}(x_1) \rangle \quad (43)$$

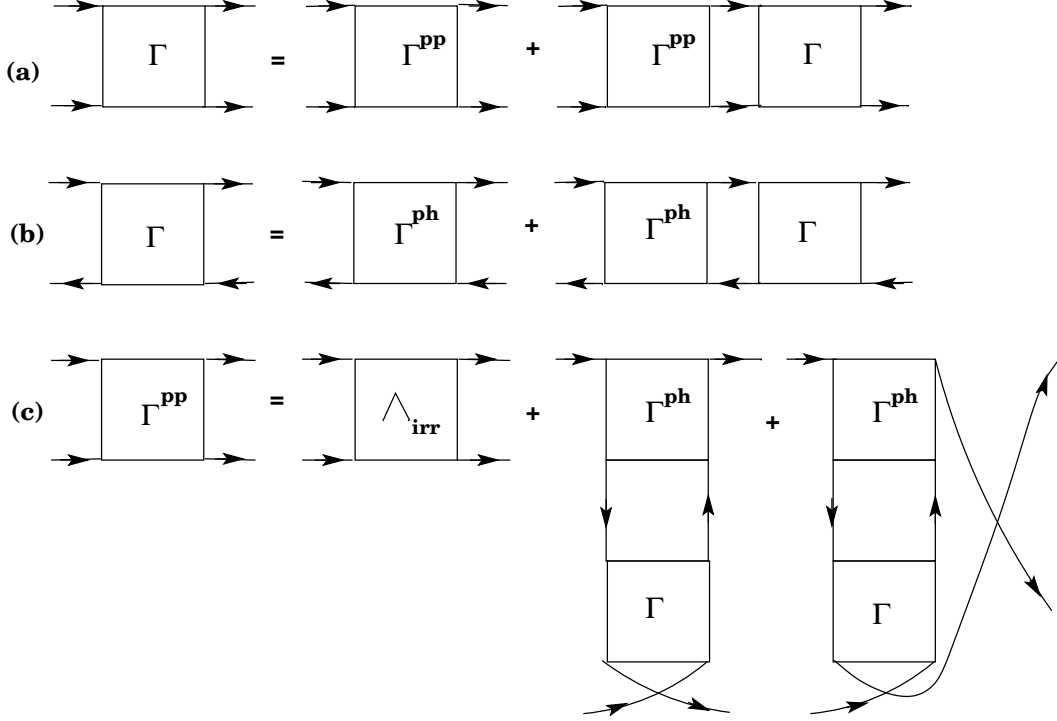


Figure 20: Bethe-Salpeter equations for (a) the particle-particle and (b) the particle-hole channels showing the relationship between the full vertex, the particle-particle irreducible vertex Γ^{pp} , and the particle-hole irreducible vertex Γ^{ph} , respectively. (c) Decomposition of the irreducible particle-particle vertex Γ^{pp} into a fully irreducible two-fermion vertex Λ_{irr} plus contributions from the particle-hole channels (Maier *et al.* [42]).

Here, $c_\sigma^\dagger(x_\ell)$ creates an electron with spin σ at site x_ℓ and imaginary time τ_ℓ . T is the usual τ -ordering operator and we have suppressed the σ indices. Fourier transforming on both the space and imaginary time variables, one obtains $G(p)$ and

$$G_2(p_4, p_3, p_2, p_1) = -G(p_1)G(p_2)(\delta_{p_1, p_4}\delta_{p_2, p_3} - \delta_{p_1, p_3}\delta_{p_2, p_4}) + \frac{T}{N} \delta_{p_1+p_2, p_3+p_4} G(p_4) G(p_3) \Gamma(p_4, p_3; p_2, p_1) G(p_2) G(p_1) \quad (44)$$

with $p = (\mathbf{p}, i\omega_n)$. Then, using the Monte Carlo results for G and G_2 , one can determine the four-point vertex Γ from Eq. (44).

Given Γ and G , one can solve the Bethe-Salpeter equations shown in Fig. 20a and b to obtain the irreducible particle-particle and particle-hole vertices Γ^{pp} and Γ^{ph} . For example, in the zero center of mass and energy channel, the particle-particle Bethe-Salpeter equation

shown in Fig. 20a gives

$$\Gamma(p'|p) = \Gamma^{\text{pp}}(p'|p) - \frac{T}{N} \sum_k \Gamma^{\text{pp}}(p'|k) G_{\uparrow}(k) G_{\downarrow}(-k) \Gamma(k|p) \quad (45)$$

with $\Gamma(p'|p) = \Gamma(p', -p'; p, -p)$. Given Γ and G , one can then determine the irreducible particle-particle vertex Γ^{pp} . This procedure is essentially the opposite of what one does in the traditional diagrammatic approach. There, one introduces an approximation for the irreducible vertex Γ^{pp} and solves Eq. (45) for Γ . Here, we use Monte Carlo results for Γ and G and solve Eq. (45) for Γ^{pp} . The Monte Carlo results for Γ satisfy crossing symmetry and $\Gamma^{\text{pp}}(p'|p)$ obtained from Eq. (45) is the effective particle-particle interaction. There is no approximation except for the fact that a finite lattice is used and one has the usual statistical Monte Carlo errors (and the small systematic finite $\Delta\tau$ errors which can be eliminated by extrapolating $\Delta\tau \rightarrow 0$).

The dominant pairing response, at low temperatures, is found to occur in the even frequency $d_{x^2-y^2}$ channel. Since this channel is even in both the relative frequency and momentum, it must be a spin singlet. Note that there are also spin singlet pairing channels which are odd in the relative frequency and momentum. However, the pairing instability in the doped Hubbard model comes from the even frequency and even momentum part of the irreducible particle-particle vertex.

$$\Gamma_e^{\text{pp}}(p'|p) = \frac{1}{2} [\Gamma^{\text{pp}}(p'|p) + \Gamma^{\text{pp}}(-p'|p)] . \quad (46)$$

Determinantal quantum Monte Carlo results [41] for $\Gamma_e^{\text{pp}}(p'|p)$ obtained from an 8×8 lattice with $U = 4t$ and $\langle n \rangle = 0.87$ are shown in Fig. 21. Here, $\Gamma_e^{\text{pp}}(p'|p)$ is plotted for various temperatures as a function of $\mathbf{q} = \mathbf{p}' - \mathbf{p}$ with $\mathbf{p} = (\pi, 0)$ and $\omega_n = \omega_{n'} = \pi T$. One sees that as the temperature is lowered, Γ_e^{pp} peaks at large momentum transfers. The size of the effective pairing interaction Γ_e^{pp} also depends upon the energy transfer $\omega_m = \omega_{n'} - \omega_n$, and falls off with ω_m on a scale set by the characteristic spin-fluctuation energy.

To obtain a more intuitive picture of the way in which the local repulsive $U n_{i\uparrow} n_{i\downarrow}$ Hubbard interaction can lead to an effective attractive pairing interaction in the singlet channel, it is

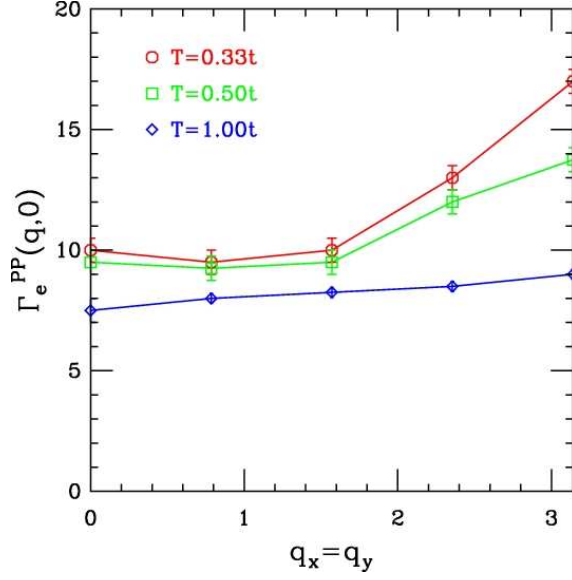


Figure 21: The even irreducible particle-particle vertex $\Gamma_e^{pp}(\mathbf{q}, \omega_m = 0)$ for $\mathbf{q} = \mathbf{p}' - \mathbf{p}$ and $\mathbf{p} = (\pi, 0)$ versus momentum transfer \mathbf{q} along the (1,1) direction. Here $U = 4t$ and $\langle n \rangle = 0.875$. As the temperature decreases below the temperature where spin-spin correlations develop, the strength of the interaction is enhanced at large momentum transfers. (Bulut *et al.* [41])

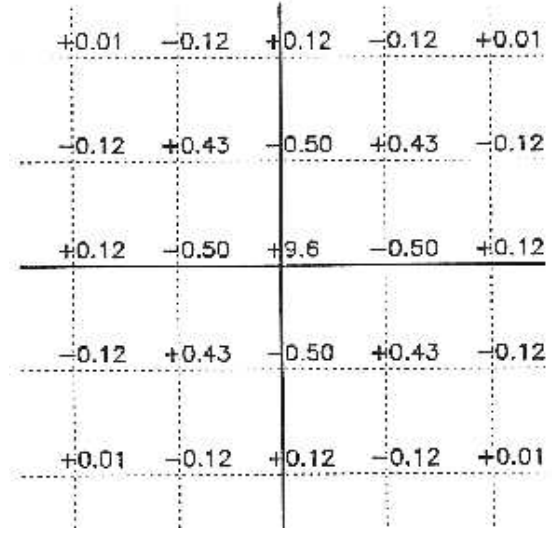


Figure 22: The real-space structure of $\Gamma_e^{pp}(\mathbf{R})$ at a temperature $T = 0.25t$ for $U = 4t$ and $\langle n \rangle = 0.87$. When the singlet electron pair is separated by one lattice spacing, $\mathbf{R} = \mathbf{x}$ or \mathbf{y} , the interaction is attractive, while it is strongly repulsive when $\mathbf{R} = 0$ and the pair occupy the same site. (Bulut *et al.* [41])

useful to construct the real space Fourier transform

$$\Gamma_e^{pp}(\mathbf{R}) = \frac{1}{N^2} \sum_{\mathbf{p}, \mathbf{p}'} e^{i(\mathbf{p}' - \mathbf{p}) \cdot \mathbf{R}} \Gamma_e^{pp}(\mathbf{p}', i\pi T; \mathbf{p}, i\pi T). \quad (47)$$

Values for $\Gamma_e^{pp}(\mathbf{R})$ are shown in Fig. 22, with the distance \mathbf{R} between the two fermions measured from the central point. If two fermions occupy the same site, spin-up and spin-down, $\Gamma_e^{pp}(\mathbf{R} = 0) \simeq 9.6t$. That is, the effective pairing interaction is even more repulsive than the bare $U = 4t$ onsite Coulomb interaction. However, if two fermions in a singlet state are on near-neighbor sites, the effective interaction $\Gamma_e^{pp}(\mathbf{R} = \hat{\mathbf{x}}$ or $\hat{\mathbf{y}}) \simeq -0.5t$ is attractive.

In order to determine the structure of the pairing correlations which are produced by

Γ_e^{PP} , we turn to the homogenous Bethe-Salpeter equation

$$-\frac{T}{N} \sum_{p'} \Gamma_e^{\text{PP}}(p|p') G_{\uparrow}(p') G_{\downarrow}(-p') \phi_{\alpha}(p') = \lambda_{\alpha} \phi_{\alpha}(p). \quad (48)$$

The temperature dependence of the leading eigenvalue in the particle-particle channel is plotted versus the temperature in Fig. 23. When this eigenvalue reaches 1, it signals an instability into a superconducting phase. Here, $U = 4t$ with $\langle n \rangle = 0.85$ and we are showing results obtained using the dynamic cluster approximation [42] for the 24-site k -cluster discussed in Section 3. The distribution of \mathbf{k} points for the 24-site cluster is shown in the inset of Fig. 23. Similar results for $T \geq 0.25t$ have been obtained using the determinantal Monte Carlo algorithm on an 8×8 lattice. [41]

The eigenfunction corresponding to the leading particle-particle eigenvalue is a singlet and its K dependence, plotted in the inset of Fig. 24, shows that it has $d_{x^2-y^2}$ symmetry. The frequency dependence of this eigenfunction at the antinodal point $K = (\pi, 0)$ is shown in the main part of Fig. 24. Here, $\phi((\pi, 0), \omega_n)$ has been normalized so that at $\omega_n = \pi T$ its value is 1. It is even in ω_n as it must be for a d-wave singlet to satisfy the Pauli principle. Also shown in this figure is the ω_m -dependence of the $Q = (\pi, \pi)$ spin susceptibility $\chi(Q, \omega_m)$ normalized by $(\chi(Q, 0) + \chi(Q, 2\pi T))/2$ for comparison with $\phi((\pi, 0), \omega_n)$. The boson Matsubara frequency dependence, $\omega_m = 2m\pi T$, of the susceptibility is seen to interlace with the fermion, $\omega_n = (2n + 1)\pi T$, dependence of the eigenfunction. The momentum and frequency dependence of $\phi_{d_{x^2-y^2}}(K, \omega)$ reflects the structure of the pairing interaction Γ_e^{PP} . The numerical results show that Γ_e^{PP} is an increasing function of momentum transfer and is characterized by a similar energy scale to that which enters the spin susceptibility $\chi(Q, \omega_m)$.

In a similar way, one can use Γ and G to solve for the irreducible particle-hole vertex Γ^{ph} shown in Fig. 20b. The homogenous Bethe-Salpeter equation for the channel with center-of-mass momentum Q , Matsubara frequency $\omega_m = 0$ and z -component of spin $S_z = 0$ is

$$-\frac{T}{N} \sum_{k'} \Gamma^{\text{ph}}(k + Q, k; k' + Q, k') G_{\uparrow}(k' + q) G_{\downarrow}(k') \phi_{Q\alpha}(k') = \lambda_{\alpha}(Q) \phi_{Q\alpha}(k). \quad (49)$$

The leading eigenvalue in the particle-hole channel occurs for $Q = (\pi, \pi)$ for the 24-site k -

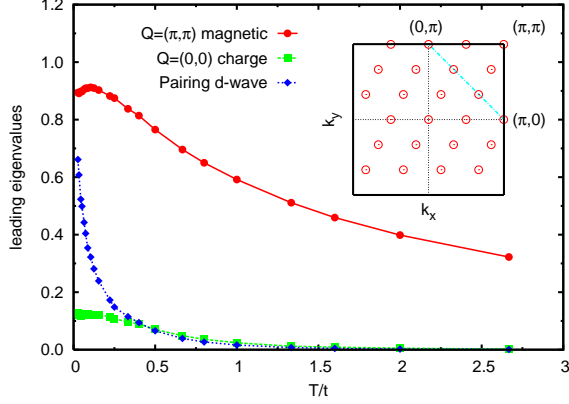


Figure 23: Leading eigenvalues of the Bethe-Salpeter equations in various channels for $U/t = 4$ and a site occupation $\langle n \rangle = 0.85$. The $\mathbf{Q} = (\pi, \pi)$, $\omega_m = 0$, $S = 1$ magnetic eigenvalue is seen to peak at low temperatures. The leading eigenvalue in the even singlet $\mathbf{Q} = (0, 0)$, $\omega_m = 0$ particle-particle channel has $d_{x^2-y^2}$ symmetry and increases toward 1 at low temperatures. The largest charge density eigenvalue occurs in the $\mathbf{Q} = (0, 0)$, $\omega_m = 0$ channel and saturates at a small value. The inset shows the distribution of k -points for the 24-site cluster. (Maier *et al.* [42])

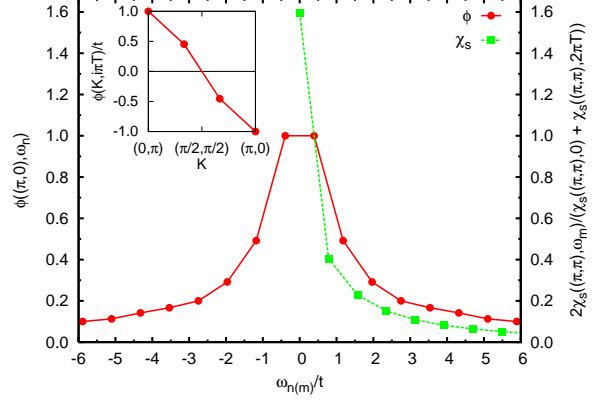


Figure 24: The Matsubara frequency dependence of the eigenfunction $\phi_{d_{x^2-y^2}}(\mathbf{K}, \omega_n)$ of the leading particle-particle eigenvalue of Fig. 23 for $\mathbf{K} = (\pi, 0)$ normalized to $\phi(\mathbf{K}, \pi T)$ (red). Here, $\omega_n = (2n + 1)\pi T$ with $T = 0.125t$. For comparison, the Matsubara frequency dependence of the normalized magnetic spin susceptibility $2\chi(\mathbf{Q}, \omega_m)/[\chi(\mathbf{Q}, 0) + \chi(\mathbf{Q}, 2\pi T)]$ for $\mathbf{Q} = (\pi, \pi)$ versus $\omega_m = 2m\pi T$ is also shown (green). In the inset, the momentum dependence of the eigenfunction $\phi_{d_{x^2-y^2}}(\mathbf{K}, \pi T)$ normalized to $\phi_{d_{x^2-y^2}}((0, \pi), \pi T)$ shows its $d_{x^2-y^2}$ symmetry. Here, $\omega_n = \pi T$ and the momentum values correspond to values of \mathbf{K} which lay along the dashed line shown in the inset of Fig. 23. (Maier *et al.* [42])

cluster and carries spin 1. Earlier determinantal quantum Monte Carlo studies [17] on 8×8 lattices show that for this doping the peak response is, in fact, slightly shifted from (π, π) , but the 24-site k -cluster used in the dynamic cluster calculation lacks the resolution to show this. As seen in Fig. 23, for this doping, the antiferromagnetic eigenvalue initially grows as the temperature is reduced, peaking at low temperatures. The largest eigenvalue in the $S = 0$ charge density channel occurs for $\mathbf{Q} = (0, 0)$ and $\omega_m = 0$. Its temperature dependence is also plotted in Fig. 23.

Returning to the question of the structure of the irreducible particle-particle vertex Γ_e^{pp} ,

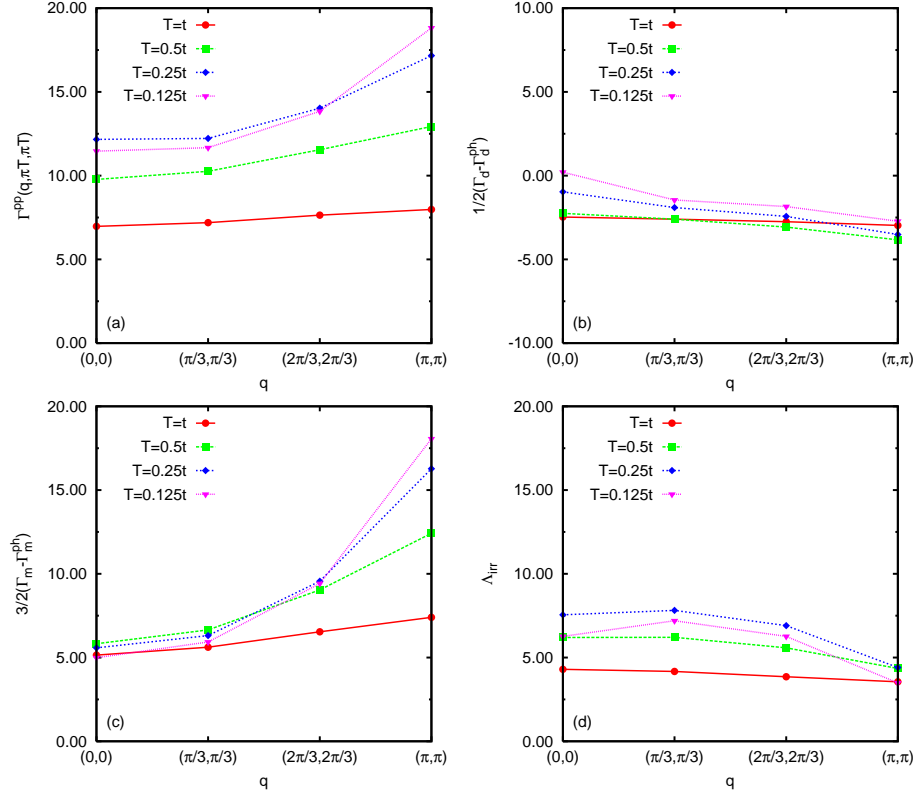


Figure 25: (a) The irreducible particle-particle vertex Γ_e^{pp} versus $\mathbf{q} = \mathbf{K} - \mathbf{K}'$ for various temperatures with $\omega_n = \omega_{n'} = \pi T$. Here, $\mathbf{K} = (\pi, 0)$ and \mathbf{K}' moves along the momentum values of the 24-site cluster which lay on the dashed line shown in the inset of Fig. 23. Note that the interaction increases with the momentum transfer as expected for a d-wave pairing interaction. (b) The \mathbf{q} -dependence of the fully irreducible two-fermion vertex Λ_{irr} . (c) The \mathbf{q} -dependence of the charge density ($S = 0$) channel $\frac{1}{2}\Phi_d$ for the same set of temperatures. (d) The \mathbf{q} -dependence of the magnetic ($S = 1$) channel $\frac{3}{2}\Phi_m$. (Maier *et al.* [42])

we have seen that Γ_e^{pp} peaks at large momentum transfers and has a frequency dependence reflected in $\Phi_{d_{x^2-y^2}}(K, \omega_n)$ which is similar to the spin susceptibility. However, we would like to understand one further aspect. Is the dominant contribution to the $d_{x^2-y^2}$ pairing interaction associated with an $S = 1$ particle-hole channel? Alternatively, for example, one could have a charge density $S = 0$ channel or a more complicated multiparticle-hole exchange process such as that suggested by the spin-bag picture. [69]

In order to address this, we will make use of the representation of Γ^{pp} shown diagrammatically in Fig. 20c. Here, Γ^{pp} is decomposed into a fully irreducible vertex Λ_{irr} plus

contribution from particle-hole exchange channels. Because of the spin rotation invariance of the Hubbard model, one can separate the particle-hole channels into a charge density $S = 0$ contribution and a spin $S = 1$ magnetic part. For the even frequency and even momentum (singlet pairing) part of the irreducible particle-particle vertex, Eq. (46), one has

$$\Gamma_e^{\text{pp}}(p'|p) = \Lambda_{\text{irr}}(p'|p) + \frac{1}{2} \Phi_d(p', p) + \frac{3}{2} \Phi_m(p', p). \quad (50)$$

The subscripts d and m denote the charge density ($S = 0$) and magnetic ($S = 1$) particle-hole channels respectively, with

$$\begin{aligned} \Phi_{d/m}(p', p) = & \frac{1}{2} \left[\Gamma_{d/m}(p' - p; p, -p') - \Gamma_{d/m}^{ph}(p' - p; p, -p') \right. \\ & \left. + \Gamma_{d/m}(p' + p; -p, -p') - \Gamma_{d/m}^{ph}(p' + p; -p, -p') \right] \end{aligned} \quad (51)$$

Here, on the right hand side, the center of mass and relative wave vectors and frequencies in these channels are labeled by the first, second and third arguments, respectively.

Results for the irreducible particle-particle interaction Γ_e^{pp} obtained from the 24-site dynamic cluster approximation are shown in Fig. 25. As we have seen, when the temperature is lowered, Γ_e^{pp} increases as the momentum transfer $\mathbf{q} = \mathbf{p}' - \mathbf{p}$ increases. Using the results for Γ^{ph} , Γ , and G one can calculate the contributions Φ_d from the $S = 0$ charge density and Φ_m for the $S = 1$ magnetic channels. Subtracting these from Γ_e^{pp} gives Λ_{irr} and results for each of these contributions are shown in Fig. 25. The dominant $d_{x^2-y^2}$ pairing contribution to Γ_e^{pp} clearly comes from the $S = 1$ channel.

At larger values of U , 4-site k -cluster calculations [70] of the temperature dependence of the $d_{x^2-y^2}$ eigenvalue for $\langle n \rangle = 0.85$ and $U = 4t, 8t$ and $12t$ are shown in Fig. 26. Over the temperature range [71] shown in Fig. 26, the $d_{x^2-y^2}$ eigenvalue is largest for $U = 8t$. This is consistent with the 2-leg ladder result shown in Fig. 13 and the expectation that the maximum transition temperature occurs for U of order the bandwidth. The $d_{x^2-y^2}$ eigenfunction $\phi_{d_{x^2-y^2}}(K, \omega_n)$ has the expected d-wave K dependence and its Matsubara frequency dependence for $U = 4t$ and $8t$ are shown in Fig. 27. Here, as before, we also show the ω_m dependence of the spin susceptibility $\chi(Q, \omega_m)$. As U increases, both $\phi_{d_{x^2-y^2}}(K, \omega_n)$

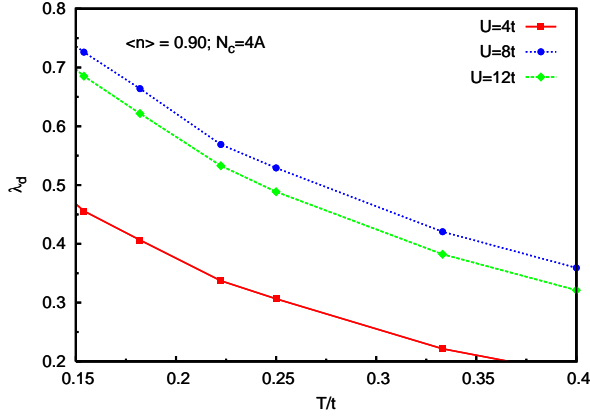


Figure 26: The $d_{x^2-y^2}$ -wave eigenvalue λ_d versus temperature T/t for $\langle n \rangle = 0.85$ with $U = 4t$ (red), $U = 8t$ (blue) and $U = 12t$ (green). These results were obtained for a 4-site k -cluster (Maier *et al.* [70]).

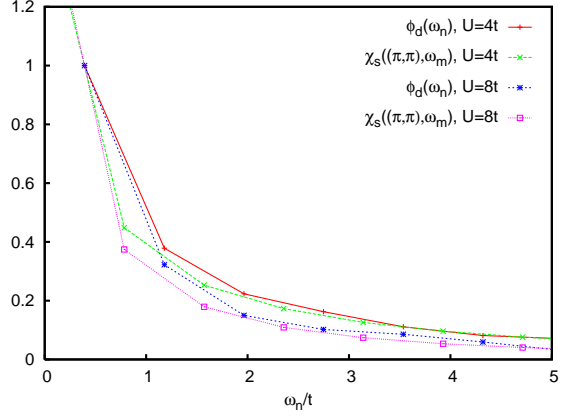


Figure 27: The Matsubara frequency dependence of the $d_{x^2-y^2}$ eigenfunction $\phi_d(K, \omega_n)$ with $K = (\pi, 0)$ for $U = 4t, 8t$ and $12t$. The spin susceptibility $\chi(Q, \omega_m)$ for $Q = (\pi, \pi)$ is also shown for comparison. Here, ϕ_d and χ are normalized in the same way as the results shown in Fig. 25 (Maier *et al.* [70]).

and $\chi(Q, \omega_m)$ fall off more rapidly, reflecting the reduction in the frequency scale set by $J \sim 4t^2/U$.

5. Conclusions

The numerical studies of the Hubbard model that we have reviewed show that it exhibits the basic properties that are observed in the cuprate materials: antiferromagnetism, $d_{x^2-y^2}$ -pairing, stripes and pseudogap phenomena. Numerical methods have also been used to study the structure of the interaction responsible for pairing in the Hubbard model. As discussed in Section 4, this can be done by directly calculating the irreducible particle-particle vertex Γ^{pp} or by studying the momentum and frequency dependence of the gap function $\phi_{d_{x^2-y^2}}(K, \omega)$. The decomposition of Γ^{pp} showed that the dominant pairing interaction arose from a spin-one particle-hole exchange. The strength of Γ^{pp} was found to increase with momentum transfer leading to $d_{x^2-y^2}$ -pairing. Alternately, the $(\cos K_x - \cos K_y)$ momentum dependence of the gap function $\phi_{d_{x^2-y^2}}(K, \omega)$ and the similarity of its ω_n dependence to that of the $Q = (\pi, \pi)$

spin susceptibility leads to the same conclusion: the pairing interaction in the doped Hubbard model is repulsive on site, attractive between near-neighbor sites and retarded on a time scale set by the inverse of the spin-fluctuation spectrum. It is important to recognize that this spectrum includes a particle-hole continuum.

Now, one can ask whether this interaction is actually the mechanism responsible for pairing in the high T_c cuprate materials and how one would know this from experiments? As far as the momentum dependence of the interaction is concerned, ARPES studies [66] of the k -dependence of the gap along with a variety of transport [72] and phase dependent studies [73,74] provide strong evidence for the nodal d-wave character of the gap. While it is known that the chains in YBCO lead to an admixture of s-wave [75–77] and the momentum regions probed are primarily along the fermi surface, there is good reason to believe from the observed k -dependence of the gap that the pairing interaction is indeed repulsive on site and attractive for singlets formed between near neighbor sites. It will be interesting to compare calculations for an orthohombic Hubbard model with experiments [76,77], to see if the observed k -dependence of the gap can provide additional help in identifying the pairing mechanism.

Another characteristic of the interaction is its frequency dependence. Here, less is known but it seems likely that the frequency dependence of the gap and renormalization parameter will provide important insight into the mechanism. As one knows, it was the frequency dependence of the gap for the traditional low T_c superconductors that provided the ultimate fingerprint identifying the phonon exchange pairing interaction, although at the time few doubted that this was the mechanism. In the high T_c case, the initial hope was that the d-wave momentum dependence of the gap would provide a sufficiently precise fingerprint. However, this has not been the case. For example, the exchange of B_{1g} phonons is known to favor d-wave pairing, [55,78], although its overall contribution to T_c is small within the standard theory. A two-band Cu-O model, in which fluctuations in circulating currents provide a d-wave pairing mechanism, has also been proposed. [79] Even within the framework of the Hubbard model there are different views regarding the dynamics. In the “Plain-

Vanilla-RVB” picture, [80] it has been suggested that the dynamics is set by an energy scale associate with the Mott-Hubbard gap. [81] However, our numerical results support a picture in which the dominant contributions come from particle-hole excitations within the relatively narrow band that the doped holes enter giving an energy scale of several times J . While the spectrum of these excitations extends down to zero energy, the main strength is associated with a broad spin-fluctuation continuum. [82,83] Thus it seems likely that the dynamics will again be important in identifying the mechanism.

In addition to the traditional electron tunneling [84] and infrared conductivity [85] measurements, ARPES experiments provide an important tool for probing the frequency dependence of the renormalization parameter and the gap. Advances in the energy and momentum resolution of both ARPES [66] and neutron scattering [86] along with material preparation techniques that allow ARPES and neutron scattering to be done on the same material are opening new opportunities. Various RPA-BCS approximations have been used to model both the ARPES [87, 88] and neutron scattering data. [89, 90] One would clearly like to extend the numerical Hubbard model studies so that they can be used in making such experimental comparisons.

Finally, in addition to the frequency and momentum dependence of the interaction, there is the question of its strength. The estimate for the transition temperature in Sec. 3 with $U = 4t$ was relatively small. As discussed, we believe that for larger values of U (of order the bandwidth) and a more optimal bandstructure, T_c will increase. Beyond this, the actual Cu-O structure has additional exchange paths and it is known that $t-J-U$ Hubbard ladders can exhibit stronger pairing correlations. [91] Nevertheless, the question of the strength of the pairing interaction remains. It is not that several times J isn’t a wide spectral range compared to the phonon scale of the traditional low temperature superconductors or that the system isn’t strongly coupled with U of order the bandwidth. Rather it is that the strong coupling has created a delicately balanced system. [92] As discussed in Sec. 3, different numerical methods on different lattices find evidence in one case for d -wave pairing and in another for stripes. Thus small changes in local parameters may alter the nature of the

correlations and there is a question regarding the role of inhomogeneity in the cuprates. An interesting theory of “dynamic inhomogeneity-induced pairing” is discussed in another chapter of this treatise. [93] In this approach, pairing from repulsive interactions appears as a mesoscopic effect and the phenomena of high temperature superconductivity is viewed as arising from the existence of mesoscale structures. [93,94] Recent STM measurements of impurities and inhomogeneities in BSCCO are providing important new information on the question of the local modulation of the pairing and its strength. [95–97]

Thus, two decades after Bednorz’ and Müller’s [98] discovery of the high T_c cuprates the question of the pairing mechanism remains open. However, it is clear that the desire to understand these materials has driven dramatic advances in the experimental energy and momentum resolution of ARPES and neutron scattering and the energy and spatial resolution of STM. It was also largely responsible for the development of a variety of numerical techniques which are providing new insights into the electronic properties of a wide class of strongly correlated materials.

Acknowledgement

I would like to acknowledge past graduate students N. Bulut, J.M. Byers, M. Jarrell, E. Loh, R. Melko, R.M. Noack, S. Quinlan, and R. Scalettar and postdocs F. Assaad, N.E. Bickers, L. Capriotti, E. Dagotto, T. Dahm, J. Freericks, M.E. Flatte, R. Fye, J. Hirsch, M. Imada, P. Monthoux, A. Moreo, M. Salkola, H.B. Schuttler and S.R. White who have been willing to teach me new things for so long. I would also like to acknowledge the pleasure I have had discussing and working on this problem with A.V. Balatsky, W. Hanke, P. Hirschfeld, S.A. Kivelson, T. Maier and D. Poilblanc. Finally I want to thank my long time collaborator R.L. Sugar for his insights and encouragement. This work was supported by NSF Grant DMR02-11166 and the Department of Energy under FG02-03ER46048.

Bibliography

- [1] E. Dagotto, *Rev. Mod. Phys.* **66**, 763 (1994).
- [2] J. Jaklic and P. Prelovsek, *Adv. Phys.* **49**, 1 (1999).
- [3] N. Bulut, *Adv. Phys.* **51**, 1587, (2002).
- [4] A. Georges, G. Kotliar, W. Krauth and M.J. Rozenberg, *Rev. Mod. Phys.* **68**, 13 (1996).
- [5] R.M. Noack and S.R. Manmana, *AIP Conf. Proc.* **789**, 93 (2005), cond-mat/0510321.
- [6] T. Maier, M. Jarrell, T. Pruschke and M. Hettler, *Rev. Mod. Phys.* **77** 1027 (2005).
- [7] A.-M.S. Tremblay, B. Kyung and D. Senechal, cond-mat/0511334.
- [8] E. Dagotto and T.M. Rice, *Science* **271**, 618 (1996).
- [9] D. Poilblanc, *Phys. Rev. B* **48**, 3368 (1993); *Phys. Rev. B* **49**, 1477 (1994).
- [10] F. Becca, A. Parola and S. Sorella, *Phys. Rev. B* **61**, R16287 (2000).
- [11] P.W. Leung, *Phys. Rev. B* **62**, R6112 (2000).
- [12] S.R. White and D.J. Scalapino, *Phys. Rev. Lett.* **81**, 3227 (1998).
- [13] S.R. White and D.J. Scalapino, *Phys. Rev. B* **60**, R753 (1999).
- [14] G. Hager, G. Wellein, E. Jeckelmann and H. Fehske, *Phys. Rev. B* **71**, 75108 (2005).
- [15] J.E. Hirsch, *Phys. Rev. B* **31**, 4403 (1985).

- [16] S.R. White, D.J. Scalapino, R.L. Sugar, E.Y. Loh, J.E. Gubernatis and R.T. Scalettar, *Phys. Rev. B* **40**, 506 (1989); S.R. White, D.J. Scalapino, R.L. Sugar, N.E. Bickers and R.T. Scalettar, *Phys. Rev. B* **39**, 839 (1989).
- [17] A. Moreo, D.J. Scalapino, R.L. Sugar, S.R. White and N.E. Bickers, *Phys. Rev. B* **41**, 2313 (1990).
- [18] A. Moreo, *Phys. Rev. B* **48**, 3380 (1993).
- [19] D.J. Scalapino, *Modern Perspectives in Many-Body Physics*, pp. 199–225, (Sixth Physics Summer School, Australian National University), ed. by M.P. Das and J. Mahanty, World Scientific (1994).
- [20] R. Preuss, W. Hanke and W. von der Linden, *Phys. Rev. Lett.* **75**, 1344 (1995).
- [21] R. Preuss, W. Hanke, C. Grober and H.G. Evertz, *Phys. Rev. Lett.* **79**, 1122 (1997).
- [22] D. Duffy, A. Nazarenko, S. Haas, A. Moreo, J. Riera and E. Dagotto, *Phys. Rev. B* **56**, 5597 (1997).
- [23] S. Sorella, G. Martins, R. Becca, C. Gazza, L. Capriotti, A. Parola and E. Dagotto, *Phys. Rev. Lett.* **88**, 117002 (2002).
- [24] V.I. Anisimov, M.A. Korotin, I.A. Nekrasov, Z.V. Pehelkina and S. Sorella, *Phys. Rev. B* **66**, 100502 (2002).
- [25] M. Potthoff, *Eur. Phys. J.*, **B32**, 429436 (2003).
- [26] C. Dahnken, M. Aichhorn, W. Hanke, E. Arrigoni and M. Potthoff, *Phys. Rev. B* **70**, 245110 (2004).
- [27] T.A. Maier, M. Jarrell, T.C. Schulthess, P.R.C. Kent and J.B. White, *Phys. Rev. Lett.* **95**, 237001 (2005).

- [28] C. Huscroft, M. Jarrell, T. Maier, S. Moukouri and A.N. Tahvildarzadeh, *Phys. Rev. Lett.* **86**, 139 (2001); A. Macridin, M. Jarrell, T. Maier and P.R.C. Kent, cond-mat/0509166.
- [29] B. Kyung, V. Hankevych, A.-M. Dare, A.-M.S. Tremblay, *Phys. Rev. Lett.* **93**, 147004 (2004); B. Kyung, S.S. Kancharla, D. Senechal, A.-M. Tremblay, M. Civelli, G. Kotliar, cond-mat/0502565.
- [30] C. Dahnken, M. Potthoff, E. Arrigoni and W. Hanke, cond-mat/0504618.
- [31] S.S. Kancharla, M. Civelli, M. Capone, D. Senechal, G. Kotliar, A.-M.S. Tremblay, cond-mat/0508205.
- [32] M. Aichhorn, E. Arrigoni, M. Potthoff and W. Hanke, cond-mat/0511460.
- [33] A.I. Lichtenstein and M.I. Katsnelson, cond-mat/9911320.
- [34] P.W. Anderson, *Science* **235**, 1196 (1987).
- [35] M. Salmhofer, *Commun. Math. Phys.* **194**, 249 (1998).
- [36] C.J. Halboth and W. Metzner, *Phys. Rev. B* **61**, 7364 (2000).
- [37] C. Honerkamp, M. Salmhofer, N. Furukawa and T.M. Rice, *Phys. Rev. B* **63**, 35109 (2001).
- [38] W.O. Putikka and M.U. Luchini, *Phys. Rev. B* **62**, 1684 (2000).
- [39] L.P. Pryadko, S.A. Kivelson, and O. Zachar, *Phys. Rev. Lett.* **92**, 67002 (2004).
- [40] T. Koretsune and M. Ogata, cond-mat/0505618.
- [41] N. Bulut, D.J. Scalapino and S.R. White, *Phys. Rev. B* **47**, R6157 (1993); *ibid. Phys. Rev. B* **50**, 9623 (1994).
- [42] T.A. Maier, M. Jarrell and D.J. Scalapino, *Phys. Rev. Lett.* **96**, 47005 (2006).

- [43] R. Blankenbecker, D.J. Scalapino and R.L. Sugar, *Phys. Rev. D* **24**, 2278 (1981).
- [44] S.R. White, *Phys. Rev. Lett.* **69**, 2863 (1992).
- [45] S.R. White, *Phys. Rev. B* **48**, 10345 (1993).
- [46] J. Hirsch, *Phys. Rev. Lett.* **51**, 1900 (1983).
- [47] E.Y. Loh, J.E. Gubernatis, R.T. Scalettar, S.R. White, D.J. Scalapino and R.L. Sugar, *Phys. Rev. B* **41**, 9301 (1990).
- [48] J.E. Hirsch and R.M. Fey, *Phys. Rev. Lett.* **56**, 2521 (1986).
- [49] M. Jarrell *et al.* , *Phys. Rev. B* **64**, 195130 (2001).
- [50] D. Betts, H. Lin and J. Flynn, *Can. J. Phys.* **77**, 353 (1999).
- [51] D.A. Huse, *Phys. Rev. B* **37**, 2380 (1988).
- [52] J.E. Hirsch and H.Q. Lin, *Phys. Rev. B* **37**, 5070 (1988).
- [53] In the infinite cluster limit, one expects that P_d will follow the low temperature Kosterlitz-Thouless behavior $P_d^{-1} \sim A \exp(-2B/(T - T_c)^{0.5})$.
- [54] R.M. Noack, N. Bulut, D.J. Scalapino and M.G. Zacher, *Phys. Rev. B* **56**, 7162 (1997).
- [55] O.K. Andersen, *J. Phys. Chem. Solids* **56**, 1573 (1995); *J. Low Temp. Physics* **105**, 285 (1996); *Phys. Rev. B* **62**, R16219 (2000).
- [56] E. Pavarini, I. Dasgupta, T. Saha-Dasgupta, O. Jepsen and O.K. Andersen, *Phys. Rev. Lett.* **87**, 47003 (2001).
- [57] T. Maier, M. Jarrell, T. Pruschke and J. Keller, *Phys. Rev. Lett.* **85**, 1524 (2000).
- [58] G.B. Martins, J.C. Xavier, L. Arrachea and E. Dagotto, *Phys. Rev. B* **64**, 180513 (2001).
- [59] P. Prelovsek and A. Ramsak, *Phys. Rev. B* **65**, 174529 (2002) and cond-mat/0502044.

- [60] S.R. White and D.J. Scalapino, *Phys. Rev. Lett.* **91**, 136403 (2003).
- [61] T. Timusk, and B. Statt, *Reports of Progress in Physics* **62**, 61 (1999).
- [62] H. Alloul, T. Ohno and P. Mendels, *Phys. Rev. Lett.* **63**, 1700 (1989).
- [63] Ch. Renner, B. Revaz, J.-Y. Genoud, K. Kadowaki and O. Fischer, *Phys. Rev. Lett.* **80**, 149 (1998).
- [64] C.C. Homes, T. Timusk, R. Liang, D.A. Bonn and W.N. Hardy, *Phys. Rev. Lett.* **71**, 1645 (1993).
- [65] J.W. Loram, K.A. Mirza, J.R. Cooper, W.Y. Liang and J.M. Wade, *J. of Superconductivity* **7**, 243 (1994).
- [66] A. Damascelli, Z. Hussain and Z.X. Shen, *Rev. Mod. Phys.* **75**, 474 (2004).
- [67] A. Moreo, S. Haas, A.W. Sandirk, and E. Dagotto, *Phys. Rev. B* **51**, 12045 (1995).
- [68] D.J. Scalapino, *Tr. J. Phys.* **20**, 560 (1996).
- [69] A. Kampf and J.R. Schrieffer, *Phys. Rev. B* **41**, 6399 (1990).
- [70] T.A. Maier, M. Jarrell and D.J. Scalapino, *Phys. Rev. B*
- [71] The eigenvalue for $U = 4t$ on the 4-site cluster lays above the result obtained for the 24-site cluster. As discussed in Section 3, this is expected because the 4-site cluster encloses just one d-wave plaquette and the embedding action does not contain pairfield fluctuations.
- [72] M. Chiao, R. Hill, C. Lupien, L. Taillefer, P. Lambert, R. Gagon and R. Fournier, *Phys. Rev. B* **62**, 3554 (2000).
- [73] D.J. Van Harlinger, *Rev. Mod. Phys.* **67**, 515 (1995).
- [74] C.C. Tsuei and J.R. Kirtley, *Rev. Mod. Phys.* **72**, 969 (2000).

- [75] K.A. Kouznetsov *et al.* , *Phys. Rev. Lett.* **79**, 3050 (1997).
- [76] H.J.H. Smilde, A.A. Golubov, Ariando, G. Rijnders, J.M. Dekkers, S. Harkema, D.H.A. Blank, H. Rogalla and H. Hilgenkamp, *Phys. Rev. Lett.* **95**, 257001 (2005).
- [77] J.R. Kirtley, C.C. Tsuei, Ariando, C.J.M. Verwijs, S. Harkema and H. Hilgenkamp, *Nature Physics*
- [78] T.P. Devereaux, T. Cuk, Z.-X. Shen and N. Nagaosa, *Phys. Rev. Lett.* **93**, 117004 (2004).
- [79] C.M. Varma, *Phys. Rev. B* **55**, 14554 (1997).
- [80] P.W. Anderson, P.A. Lee, M. Randeria, T.M. Rice, N. Trivedi and F.C. Zhang, *J. Phys. Condens. Matter* **16**, R755 (2004).
- [81] P.W. Anderson, cond-mat/0512471.
- [82] D.J. Scalapino, *Phys. Rep.* **250**, 330 (1995).
- [83] A.V. Chubukov, D. Pines and J. Schmalian, chapter in *The Physics of Conventional and Unconventional Superconductors* (edited by K.H. Bennemann and J.B. Ketterson, Springer-Verlag, 2002).
- [84] B. Barbiellini, O. Fischer, A.D. Kent, D.B. Mitzi and A. Kapitulnik, *Physics B* **194**, 1689 (1994).
- [85] J.P. Carbotte, E. Schachinger and D. Basou, *Nature (London)* **401**, 354 (1999).
- [86] S. Pailhes, C. Ulrich, R. Fauque, V. Hinkov, Y. Sidis, A. Ivanov, C.T. Lin, B. Keimer and P. Bourges, cond-mat/0512634.
- [87] M. Eschrig and M.R. Norman, *Phys. Rev. B* **67**, 144503 (2003).
- [88] T. Dahm, P.J. Hirschfeld, D.J. Scalapino and L. Zhu, *Phys. Rev. B*
- [89] N. Bulut and D.J. Scalapino, *Phys. Rev. B* **53**, 5149 (1996).

- [90] J. Brinckmann and P.A. Lee, *Phys. Rev. B* **65**, 14502 (2002).
- [91] S. Daul, D.J. Scalapino and S.R. White, *Phys. Rev. Lett.* **84**, 4188 (2000).
- [92] D.J. Scalapino, *Physics in Canada* **56**, 267 (2000).
- [93] S.A. Kivelson and E. Fradkin, cond-mat/0507459.
- [94] V.J. Emery and S.A. Kivelson, *Phys. Rev. Lett.* **74**, 3253 (1995); E. Arrigoni, E. Fradkin and S.A. Kivelson, *Phys. Rev. B* **69**, 214519 (2004).
- [95] A. Yazdani, C.M. Howald, C.P. Lutz, A. Kapitulnik, and D.M. Eigler, *Phys. Rev. Lett.* **83**, 176 (1999).
- [96] E.W. Hudson, S.H. Pan, A.K. Gupta, K.-W. Ng, and J.C. Davis, *Science* **285**, 88 (1999).
- [97] S.H. Pan, E.W. Hudson, K.M. Lang, H. Eisaki, S. Uchida, and J.C. Davis, *Nature* **403**, 746 (2000).
- [98] J.G. Bednorz and K.A. Müller, *Z. Phys. B: Condens. Matter* **64**, 189 (1986).

Addendum

This manuscript was written almost a year ago and will appear as Chapter 13 in the “Handbook of High Temperature Superconductivity,” edited by J.R. Schrieffer and published by Springer. It is narrowly focused on the results obtained from numerical studies of one particular model, the Hubbard model. Here in this addendum [1] I would like to briefly address the more general questions of why the quest to understand the mechanism responsible for superconductivity in the high T_c cuprates is important and where are we twenty years after Bednorz’s and Muller’s seminal discovery? As part of this, I will indicate how the numerical results for the Hubbard model may help to provide some answers.

It has been suggested [2] that the answer to the first question is that we need to “domesticate the goat.” That is, roughly 11,000 years ago man domesticated the wolf. During

the next 4000 years, different wolf species as well as various breeds of dogs were created and improved. But then, 7000 years ago the goat was discovered and domesticated. This achievement led within the next 1000 years to the domestication of sheep, cattle, chickens, swine, etc. and to a fundamentally different way of life. So the high T_c cuprate problem or, more generally, the problem of the strongly correlated electron superconductors is the goat and we are seeking to domesticate it. The hope is that this will lead to the development of new strongly correlated superconducting materials and a deeper understanding of a variety of existing ones.

A short list of some of the materials [3] discussed at the M2S-HTS Dresden meeting which fall into the category of strongly correlated superconductors follow:

Cuprates (hole and electron doped)

Heavy fermions (U_2 (PdPt)₃ B, CeCoIn₅, PrOs₄ Sb₁₂, PuCoGa₅)

Ruthenates Sr₂RuO₄

Organics κ BEDT, (TMTSF)₂PF₆

Cobaltates Na_xCoO₂ (1.3 H₂O)

In addressing the second question regarding where are we with respect to understanding the mechanism responsible for superconductivity in the cuprates, it is useful to think back to a little over a decade ago. At that time a key question involved the symmetry of the gap. At an APS March meeting, Bertrum Batlogg was asked when we would have an experiment which would tell us the symmetry of the cuprate gap. His response was quick and to the point: We already have a number of such experiments, we just don't agree on which one is correct. As it turned out, we were not so far away from settling this question. At that time, van Harlingen and his group at the University of Illinois and Tsuei, Kirtley and their co-workers at IBM were carrying out phase sensitive experiments which would provide convincing evidence that the cuprate gap was d-wave like (for orthorhombic systems $d+as$).

I believe that now, a decade later, the question regarding the nature of the cuprate pairing mechanism is at a similar stage. That is, as seen from the talks presented at this conference, there are clearly a number of theoretical proposals for the underlying cuprate pairing mechanism. Here is a short list, which I realize is incomplete (there were some 200 theoretical talks and 700 posters covering electronic structure, many-body theories, phenomenology, and proposals for experiments and new materials):

Jahn-Teller bipolarons

Stripes (the role of inhomogeneity)

RVB-RMFT-Gutzwiller Projected BCS

Electron-phonon+U

Spin-fluctuations

Charge-fluctuations

Electric quadrupole fluctuations

Loop current fluctuations

dDW, dCDW

Quantum critical point fluctuations

Competing phases

Pomeranchuk instabilities

d-to-d electronic excitations

The problem regarding the pairing mechanism is therefore reminiscent of the earlier gap symmetry question. It is not that there is a lack of proposals, but rather it is that we do not have a consensus on which one contains the appropriate description. Some of us had

thought that the experimental observation of a d-wave gap, which had been predicted from the analysis of Hubbard and t-J models, would have provided “convincing” evidence that the pairing arose from a spin mediated interaction. But as we now know, a $d_{x^2-y^2}$ gap is not a sufficiently unique signature. There are a number of possible pairing mechanisms such as B_{1g} phonons, fluctuating current loops, as well as others which may drive d-wave pairing. In addition, there is the suggestion that the pairing interaction is amplified by intrinsic inhomogeneities or stripes. There is also the question of the possible role of amplification that may be obtained near a quantum critical point (QCP). Although, I believe that this latter QCP scenario can be viewed as tuning the parameters to optimize a given pairing mechanism, much as what was done when T_c was increased in the electron-phonon systems by varying the composition in order to be near a lattice instability. In any event, the question remains, how will we know? Let’s consider some possibilities.

Perhaps it will be shown that there is another ordered phase associated with the pseudogap regime such as a d-DW or a d-CDW, a time reversal breaking current-loop phase (recent neutron scattering and Kerr effect experiments), a non-superconducting xy-like phase (non-analytic dependence of the magnetization as $H \rightarrow 0$ at temperatures above T_c), an exotic spin-liquid phase, ... There were in fact both theoretical and experimental talks on such phases, and definitive evidence for a new ordered phase would certainly narrow the theoretical possibilities. Here however it is interesting to note that in spite of the evidence for a striped phase in $\text{La}_{1.35}\text{Sr}_{0.25}\text{Nd}_{0.4}\text{CuO}_4$ and increasing evidence for stripe-like fluctuations in the cuprates, the question of whether stripes, or other intrinsic inhomogeneities, play an essential role in the high T_c pairing mechanism remains open. We did hear about ARPES experiments on $\text{La}_{2-x}\text{Sr}_x\text{CuO}_4$ which found that the gap peaks near $x = 1/8$ where T_c dips. Further experiments on dynamic inhomogeneity-induced pairing and the role of mesoscale structures in the high T_c problem are needed.

Perhaps we will know when we have a further understanding of the clues coming from the electronic structure calculations regarding the variation of T_c with the chemical structure and the effective band parameters such as the next near neighbor hopping t' . Perhaps the

insight we need will come from an understanding of the local density of states measured by STM and its relation to nearby local structural and chemical changes. Perhaps the ARPES, INS and STM studies will show that phonons play an important role. If this is the case, it seems likely that it will not be in the traditional way they do in the low T_c metals, but rather in combination with the stripes or mesoscale structures.

It may be, as suggested at this meeting, that one can identify a quantum critical point (QCP) which is associated with superconductivity and then from the nature of the QCP, identify the fluctuations which mediate the pairing. Of course if the interplay between the various phases is sufficiently strong, one may have to reconsider the meaning of mechanism.

One route that has been discussed is that of identifying the cuprate pairing mechanism by showing the similarity of the cuprates to other classes of materials which exhibit unconventional superconductivity such as the actinide metals (PuCoGa_5 , PuRhGa_5) and the heavy fermion systems (CeRIn_5 , $\text{R}=\text{Co,Rh,Ir}$). Perhaps there is a common mechanism which is tunned as one moves from one system to another. The candidate mechanism discussed at this meeting was spin-fluctuations.

Another approach is based on using numerical techniques (or possibly experimental cold atom analogues) to study particular models such as the Hubbard model. Here the idea is to determine first whether a given model exhibits the phenomena seen in the cuprates and then, if it does, determine the nature of the pairing interaction in the model. (This is the approach taken in this chapter.)

Perhaps the best approach will be to follow the path taken for the traditional low temperature superconductors where the structure of the pairing interaction was determined from the tunneling dI/dV characteristic. Here of course one knew how to get $\Delta(\omega)$ from dI/dV and had the Eliashberg theory to determine the interaction from $\Delta(\omega)$. For the cuprates one will likely need a combination of numerical and analytic approaches along with ARPES, INS, STM and conductivity data to carry out such a program.

For the cuprates, the k dependence of the gap near the fermi surface is known from a variety of experiments. A detailed map for YBCO is now available from π -junction in-

terference measurements which find an anisotropic $d+\alpha s$ wave form. If one had a simple $(\cos k_x - \cos k_y)$ form over the entire Brillouin zone, one would know that the pairing arose from an attractive near-neighbor interaction. While it is likely somewhat more extended and, for the case of an orthorhombic crystal, anisotropic, the simple d-wave form is a reasonable starting point. What is needed are experimental determinations of the frequency dependence of the gap. Actually one would like to determine both the renormalization parameter $Z(k, \omega)$ and $\Delta(k, \omega) = \phi(k, \omega)/Z(k, \omega)$ with $\phi(k, \omega)$ the gap parameter. Studies aimed at extracting the frequency dependence of the gap and the underlying interaction using conductivity $\sigma(\omega)$ as well as INS and ARPES data were reported. One can expect further progress in this direction as such data becomes available on the same crystals.

So at the present time, the question of the mechanism responsible for pairing in the high T_c cuprates remains open. However, it is clear from the work presented at this conference that we are moving closer to an understanding.

Bibliography

- [1] This addendum is based upon a closing “Theory Summary” from the 8th International Conference on Materials and Mechanisms of Superconductivity and High-Temperature Superconductors (M2S-HTS) held in Dresden, July 8–16, 2006. References associated with many of these remarks appear in the conference proceedings which will be published in *Physica C* by Elsevier Science. I also benefited from insights obtained in discussions with colleagues.
- [2] I. Manzin, DOE meeting on Basic Research Needs for Superconductivity, Washington, DC, May 8–11, 2006.
- [3] In addition, there were a number of talks about the sigma-orbital materials such as MgB_2 , Li (high pressure form) and doped diamond, which are of great interest but are driven by electron-phonon interactions and do not appear to be directly related to the cuprate problem.